Solid Earth Discuss., https://doi.org/10.5194/se-2019-86
Manuscript under review for journal Solid Earth
Discussion started: 22 May 2019

Anatomy of the magmatic plumbing system of Los Humeros Caldera (Mexico): implications for geothermal systems

Federico Lucci[1, *], Gerardo Carrasco-Núñez[2], Federico Rossetti[1], Thomas Theye[3], John C. White[4], Stefano Urbani[1], Hossein Azizi[5], Yoshihiro Asahara[6], and Guido Giordano[1, 7]

[1]Dipartimento di Scienze, Sez. Scienze Geologiche, Università Roma Tre, Largo S. L. Murialdo 1, 00146 Roma, Italy
[2]Centro de Geociencias, Universidad Nacional Autónoma de México, Campus UNAM Juriquilla, 76100, Queretaro, Mexico
[3]Institut für Anorganische Chemie, Universität Stuttgart, Stuttgart, Germany
[4]Department of Geosciences, Eastern Kentucky University, Richmond, KY 40475, USA
[5]Mining Department, Faculty of Engineering, University of Kurdistan, Sanandaj, Iran
[6]Department of Earth and Environmental Sciences, Graduate School of Environmental Studies, Nagoya University, Nagoya 464-8601, Japan
[7]CNR - IDPA, Via Luigi Mangiagalli 34, 20133 Milano
*Corresponding Author e-mail: federico.lucci@uniroma3.it

Solid Earth Discuss., https://doi.org/10.5194/se-2019-86
Manuscript under review for journal Solid Earth
Discussion started: 22 May 2019

ABSTRACT

Understanding the anatomy of magma plumbing systems of active volcanoes is essential not only for unraveling magma dynamics and eruptive behaviors, but also to define the geometry, depth and temperature of the heat sources for geothermal exploration. The Pleistocene-Holocene Los Humeros volcanic complex is part of the Eastern Trans-Mexican Volcanic Belt (Central Mexico) and it represents one of the most important exploited geothermal fields in Mexico with *ca*. 90 MW of produced electricity.

A field-based petrologic and thermobarometric study of lavas erupted during the Holocene (post-Caldera stage) has been performed with the aim to decipher the anatomy of the magmatic plumbing system existing beneath the caldera. New petrographical, whole rock major element data and mineral chemistry were integrated within a suite of inverse thermobarometric models. Compared with previous studies where a single voluminous melt-controlled magma chamber (or "Standard Model") at shallow depths was proposed, our results support a more complex and realistic scenario characterized by a heterogeneous multilayered system comprising a deep (*ca*. 30 km) basaltic reservoir feeding progressively shallower and smaller distinct stagnation layers, pockets and batches up to very shallow conditions (1kbar, *ca*. 3km). Evolution of melts in the feeding system is mainly controlled by differentiation processes via fractional crystallization, as recorded by polybaric crystallization of clinopyroxenes and orthopyroxenes.

Moreover, this study attempts to emphasize the importance to integrate field-petrography, texture observations and mineral chemistry of primary minerals to unravel the pre-eruptive dynamics and therefore the anatomy of the plumbing system beneath an active volcanic complex, which notwithstanding the numerous existing works is still far to be well understood. A better knowledge of the heat source feeding geothermal systems is very important to improve geothermal exploration strategies.

Keywords

Magmatic plumbing system, Thermobarometry, Calderas, Los Humeros, Trans Mexican Volcanic Belt, heat source, geothermal exploration

1.INTRODUCTION

Recent views on the structure of volcanic plumbing systems have deeply changed, moving from the "Standard Model" (*sensu* Gualda and Ghiorso, 2013) of a single, bowl-shaped magma chamber inside which all petrologic processes of differentiation and assimilation occur (e.g. Hildreth, 1979, 1981; Hildreth and Wilson, 2007) to more complex arrays of stratified and variably interconnected of transient magma accumulation zones, set in largely crystallized and vertically extensive mush zones (e.g., Bachman and Bergantz, 2004; 2008; Cashman and Giordano, 2014; Cashman et al., 2017). Furthermore, the time required for the assembly of large magma chambers is now believed to be very short, in terms of decades to few thousands of years for tens to hundreds of km^3 of eruptible magma (e.g. Glazner, 2004; Charlier et al., 2007), which are then rapidly evacuated during eruptions of caldera forming ignimbrites (e.g., Begué et al., 2014; Rivera et al., 2014; Wotzlaw et al, 2014; Matthews et al., 2015; Carrasco-Núñez et al., 2018). Key factors in determining the internal architecture of the magmatic systems is the magma intrusion rate that controls whether successive pulses of magma will coalesce to form progressively larger chambers, as well as the formation of ductile shells surrounding the magma chamber that prevent country rock failure, favoring the inflation of the reservoir (Jellinek and de Paolo, 1981; Annen, 2009). Numerical simulations suggest that caldera systems smaller than 100 km^2 are feed by plumbing systems encapsulated by country rocks that remain sufficiently brittle, while larger systems are more ductile favoring increase in size (Gregg et al., 2012).

The implications of such innovative conceptual models on the modeling of the heat source in magmatic-bearing geothermal systems are profound. Nonetheless, common numerical modeling of conductive-convective heat transfer in caldera-related geothermal systems have commonly envisaged the classic magma chamber as a single body, more or less chemically stratified entirely at magmatic temperatures, whose dimensions and depths have been usually constrained by volcanological and petrological data (e.g. Verma, 1985; Wohletz et al., 1999). More complex modeling requires the "unpacking" of the stratigraphy of a volcano by the identification of the various "magma chambers" or magma storage layers that fed the different eruptions over time and space (e.g., Di Renzo et al., 2016).

A key to decipher where magmas are stored and, therefore, the anatomy of a magmatic plumbing system, is the understanding of pre-eruptive processes such as mineral crystallization, migration and stagnation of melts prior to their eruption (Feng and Zhu, 2018, Putirka, 2008; Keiding and Sigmarsson, 2012; Scott et al., 2012, Barker et al., 2015; Jeffery et al., 2013; Cashman and Giordano, 2014; Pamukcu et al., 2015;Lucci et al., 2018). As a matter of fact, early segregated minerals reflect the magmatic environment (i.e., pressure – temperature – magma/fluid composition, oxidation state) and, therefore, with their growth, texture and chemistry provide an important archive of information (Feng and Zhu, 2018; Ginibre et al., 2007; Giuffrida and Viccaro, 2017; Viccaro et al., 2016; Putirka et al., 2008; Lucci et al., 2018). Accordingly, petrographic observations and mineral chemistry of primary minerals, integrated with opportunely selected

thermobarometry models (e.g., Putirka, 2008; Masotta et al., 2013) could lead to the comprehension and reconstruction of the magmatic storage/feeding systems of the erupted products (Feng and Zhu, 2018; Giuffrida and Viccaro, 2017; Elardo and Shearer, 2014; Petrone et al., 2016; Zheng et al., 2016; Eskandari et al., 2018; Shane and Coote, 2018; Scott et al., 2012; Stroncik et al., 2009; Barker et al., 2015; Jeffery et al., 2013; Keiding and Sigmarsson, 2012).

In this paper we present a geothermobarometric study of the post-caldera, Pleistocene-Holocene products of Los Humeros volcanic complex (LHVC), at the eastern termination of the Neogene-Quaternary Trans-Mexican Volcanic Belt (TMVB) (Fig. 1) in order to reconstruct the present-day geometry and structure of the magmatic plumbing system, necessary to build up a conceptual model for the magmatic heat source of the active and currently exploited geothermal system. The magmatic heat source for LHVC has been constrained by the geometry of the caldera, the volume and mass balance calculations of the associated ignimbrites (Ferriz and Mahood, 1984, 1987; Verma, 1984, 1985a, 1985b, Verma et al., 1990; Verma and Andaverde, 1995; Verma et al., 2011; Verma et al. 2013), all related to a single magma body. Our results indicate that the present configuration of the plumbing system is vertically extensive and extends across the entire crust comprising a deeper residence zone for basalts at ca. 30 km and a complex middle to upper crust zone where smaller batches of magma differentiate to trachyandesites and trachytes at times interconnected with the lower feeding zone. The main outcome for the modeling of the magmatic heat source of the geothermal system is the rejection of conservative conceptual models based on the classical melt-dominated, single, voluminous, long-lived magma chamber, and the proposal of a new and more realistic vision of the magmatic plumbing systems made of multiple interconnected magma stagnation layers within the crust. The results and approach presented in this work have a general value and could represent an efficient strategy to explore and reconstruct, through petrological investigation, the pre-eruptive geometry and the anatomy of magmatic feeding systems. These findings in turn, must be considered into the new conceptual geothermal models to improve strategies for geothermal exploration.

2.GEOLOGICAL SETTING

2.1 Regional Geology

LHVC is the largest and easternmost Quaternary caldera (Fig. 1) of the 1200 km-long active continental arc of the Trans-Mexican Volcanic Belt (TMVB), generated since *ca.* 20 Ma by the subduction of Cocos plate beneath central Mexico (e.g. Demant, 1978, Ferrari et al. 1999, 2012; Gomez-Tuena et al., 2003, 2007a, 2007b, 2018; Norini et al., 2015). LHVC is located in the eastern sector of the TMVB, which is characterized by monogenetic volcanism, scattered basaltic cinder and scoria cones, maar volcanoes of basaltic and rhyolitic composition, large rhyolitic domes and major stratovolcanoes such as Pico de Orizaba (or Citlaltépetl) and Cofre de Perote (e.g., Yáñez and García, 1982; Negendank et al., 1987; Carrasco-Núñez et al., 2010, 2012a;).

The Paleozoic to Mesozoic crystalline basement of eastern TMVB is exposed along the Teziutlán Massif (Viniegra, 1965; Ferriz and Mahood, 1984) made of metamorphic (greenschists K-Ar dated at 207 ± 7 Ma, in Yáñez and García, 1982) and intrusive (granodiorites and granites with whole-rock K-Ar ages of 246 ±7 Ma and 181 ±5 Ma, Yáñez and García, 1982) rocks. The crystalline basement is partially covered by a thick, highly deformed Mesozoic sedimentary succession part of the Sierra Madre Oriental NW-SE thrusts and folds belt formed by the Late Cretaceous to Paleocene compressional Laramide Orogeny (e.g. Campos-Enriquez and Garduño-Monroy, 1987; Suter, 1987; Fitz-Díaz et al., 2018). Oligocene to Miocene granodiorite and syenite intrusions are randomly exposed within the area (whole-rock K-Ar ages of 31-15 Ma, Yáñez and García, 1982). Miocene volcanism in the area is represented by andesites of the Cerro Grande volcanic complex (Gómez-Tuena and Carrasco-Núñez, 2000), dated at 8.9 to 11 Ma (K/Ar method on whole-rock, Carrasco-Núñez et al. 1997), and the Cuyoaco Andesite dated at 10.5 Ma (K/Ar method, Yáñez and García, 1982) to the west of LHVC, which may correlate with the Alseseca Andesite (Yáñez and García, 1982) exposed to the north. Neogene andesitic volcanism (Ferriz and Mahood, 1984; Yáñez and García, 1982) represented by the Teziutlán Andesite, K-Ar dated (whole-rock) between 3.5 and 5 Ma by Yáñez and García (1982) and at 1.55 Ma by Ferriz and Mahood (1984). This andesitic activity was recently dated by the $^{40}Ar/^{39}Ar$ method at 2.61-1.46 Ma (Carrasco-Núñez et al., 2017a) and correlates with most of the thick andesitic successions of the subsurface geology of LHVC.

2.2 Los Humeros Volcanic Complex

The volcanic evolution of the LHVC consists of three main stages (Carrasco-Núñez et al., 2018): (i) pre-caldera stage; (ii) caldera stage; and (iii) post-caldera stage. The pre-caldera stage is represented by relatively abundant rhyolitic domes, which erupted mainly to the western side of Los Humeros caldera, with an isolated spot to the south, and some buried lavas identified in the geothermal well-logs (Carrasco-Núñez et al., 2017a). This volcanism has been recently dated by both U-Th and $^{40}Ar/^{39}Ar$ methods (Carrasco-Núñez et al., 2018), providing ages spanning from 693.0±1.9 ($^{40}Ar/^{39}Ar$, plagioclase) to 270±17 ka (U/Th, zircon), which overlap with the age range obtained from other domes of the western sector outside the caldera, where K-Ar ages (sanidine) of 360±100 ka and 220±40 ka were obtained (Ferriz and Mahood, 1984). The Caldera stage consists of two major caldera-forming events, separated by a large Plinian eruptive episode. The first and largest caldera-forming eruption produced Los Humeros caldera (18 km in diameter) during the emplacement of the Xaltipan ignimbrite, a rhyolitic, welded to non-welded, ash-rich deposit, radially distributed around the caldera. The dense rock equivalent (DRE) volume of this event was estimated at 115 km^3 by Ferriz and Mahood (1984). The age of the Xaltipan ignimbrite was established by whole-rock K-Ar dating at 460±20 ky (plagioclase) and 460±130 ky (biotite) (Ferriz and Mahood, 1984), however Carrasco-Núñez et al. (2018) based on coupled zircon U-Th dating and $^{40}Ar/^{39}Ar$ method (plagioclase) geochronology provided a younger age of 164.0 ± 4.2 ka.

Solid Earth Discuss., https://doi.org/10.5194/se-2019-86
Manuscript under review for journal Solid Earth
Discussion started: 22 May 2019

Following this catastrophic event an eruptive pause occurred, resuming with a sequence of intermittent Plinian episodes at 70±23 ka ($^{40}Ar/^{39}Ar$ method on plagioclase, Carrasco-Núñez et al., 2018), separated by short gaps marked by thin paleosoils. The deposits consist of thick (1-6 m) coarse pumice-rich, well-sorted, massive and diffuse-stratified layers,rhyodacitic in composition, which are grouped as the Faby Tuff (Ferriz and Mahood 1984; Willcox, 2011). The second caldera-forming episode produced the 9-10 km large Los Potreros caldera, which is associated with the emplacement of the compositionally-zoned andesitic-rhyodacitic-rhyolitic Zaragoza ignimbrite (Carrasco-Núñez et al., 2012b). This is an intraplinian pyroclastic flow deposit, with an estimated volume of ca. 15 km3 DRE (Carrasco-Núñez and Branney, 2005). Previous ages of this unit were reported at 100 ka (K-Ar dating, plagioclase: Ferriz and Mahhod, 1984) and at 140±24 ka ($^{40}Ar/^{39}Ar$ method, plagioclase: Willcox, 2011). However, a new $^{40}Ar/^{39}Ar$ (on plagioclase) younger age of 69±16 ka for the Zaragoza ignimbrite was recently obtained (Carrasco-Núñez et al., 2018), confirmed by the fact the Zaragoza ignimbrite overlies a rhyodacitic lava flow dated at 74.2±4.5 ka (zircon U-Th dating).

According to Carrasco-Núñez et al. (2018) during the post-caldera stage (Fig. 1) two different eruptive phases occurred. The first one was a late Pleistocene resurgent phase characterized by the emplacement of felsic domes in the central area at about 44.8±1.7 ka (zircon U-Th ages; Carrasco-Núñez et al., 2018), which is slightly younger than the previously reported whole-rock K-Ar date (60±20 ka, glass: Ferriz and Mahood, 1984). Outside of the caldera, to the north, a rhyolitic dome erupted at 50.7±4.4 ka ($^{40}Ar/^{39}Ar$, plagioclase; Carrasco-Núñez et al., 2018), which was followed by a sequence of explosive eruptions, producing dacitic pumice fall units (Xoxoctic Tuff, 0.6 km^3) and interbedded breccia and pyroclastic flows deposits of the Llano Tuff (Ferriz and Mahood 1984; Willcox, 2011), with a maximum age of 28.3±1.1 ka (C-14, Cal BP 30630, Rojas-Ortega, 2016). The second eruptive phase of the post-caldera stage is a Holocene ring-fracture and bimodal phase that occurred towards the south, north and central part of Los Humeros caldera (Carrasco- Núñez et al., 2017). It is characterized by alternated episodes of effusive and explosive volcanism with a wide range of compositions, spanning from basaltic-andesitic,basaltic trachytic, trachyandesitic lava flows and dacitic, trachydacitic, andesitic and basaltic pumice and scoria fall deposits erupted by tens of monogenetic eruptive centers located in the LHVC (Ferriz and Mahood, 1984; Dávila-Harris and Carrasco-Núñez, 2014; Norini et al., 2015; Carrasco-Núñez et al., 2017b). Most of the effusive activity was firstly considered within a range of 40-20 ka (whole-rock K-Ar dating, Ferriz and Mahood, 1984), however, recent dating reveals that most of this activity is Holocene (Carrasco et al., 2017b). Trachyandesitic and andesitic basalts lavas erupted to the north of the LHVC at about 8.9±0.03 ka (C-14 age, Carrasco-Núñez et al, 2017b). A rhythmic alternation of contemporaneous bimodal explosive activity produced trachyandesitic and basaltic fall layers grouped as the Cuicuiltic Member erupted at 7.3±0.1 ka (C-14 age,Dávila-Harris and Carrasco-Núñez, 2014). This activity migrated towards the southern caldera rim to forms a well-defined lava field. This ring-fracture episode erupted trachyandesite and olivine-bearing basaltic lava flows, at 3.9±0.13 ka (C-14 age, Carrasco-Núñez et al, 2017b), and the most recent eruptions

erupted trachytic lava flows near the SW caldera rim, at 2.8± 0.03 ka (C-14 age, Carrasco-Núñez et al, 2017b).

2.3 Los Humeros geothermal system

The LHVC hosts one of the three most important geothermal fields in Mexico, with an installed 93 MW of electric power produced from 20 geothermal wells (Romo-Jones et al., 2017). The existing conceptual models for the Los Humeros geothermal field (LHGF) (see Norini et al., 2015 for a review) stem upon the hypothesis of a unique, large and voluminous cooling magma chamber of 1000-1500 Km^3 in volume, at depth of 5 to 10 km from the surface (Verma, 1984, 1985a, 1985b, 2000; Verma et al., 1990; Verma and Andaverde, 1995; Verma et al., 2011; Verma et al. 2013; Carrasco-Núñez et al. 2018), representing the heat source of the geothermal field (Martínez et al., 1983; Verma, 1983, 2000; Campos-Enríquez and Garduño-Monroy, 1987). However, the LHGF is characterized by a low number of productive geothermal wells (ca. 20 out of 50; Norini et al., 2015; Carrasco-Núñez et al., 2017a). The confined distribution of these productive wells along the NNW-SSE trending "Maxtaloya-Los Humeros-Loma Blanca" fault system (MHBfs in Fig. 1) cutting across the Los Potreros caldera (e.g., Norini et al., 2015; Carrasco-Núñez et al., 2017a) also corresponds to the almost unique, narrow and sharp surface thermal anomaly recognized within the caldera (Norini et al., 2015). These observations raise doubts on the existence of a voluminous superficial heat source feeding the LHGF and makes it important, for a better comprehension and exploitation of the geothermal resource, a revised assessment of the structure of the magmatic plumbing system beneath LHVC.

3.MATERIALS AND METHODS

In this work we focus on petrographical investigations, textural and chemical (mineral chemistry and major-elements bulk-rock) characterization of the Los Humeros post-caldera stage (LHPCS) (Carrasco-Núñez et al. 2017b). Following the recently published geological map (Carrasco-Núñez et al. 2017b) and geochronology (Carrasco-Núñez et al. 2018) of the LHVC, a number of thirteen samples of the LHPCS lavas were collected in the field (Fig. 1), with the aim to describe all the compositional variability of erupted products during the post-caldera stage activity (Figs. 1, 2a-d). In the description of the volcanic units, abbreviations follow Carrasco et al. (2017b). Concerning the extra-caldera products (Fig. 2d), we collected samples from all the four major lava flows: (i) LH15 from El Limón lava flow (Qab), (ii) LH21-2 from Sarabia lava flow (Qta1), (iii) LH17 from Tepeyahualco lava flow (Qtab), and (iv) LH18 from Texcal lava flow (Qb1).

With respect to the intra-caldera domain (Fig. 2a), we sampled lavas belonging to: (i) LH27-1 from the mafic lavas inside the Xalapasco Crater (Qb1), (ii) LH27-2 from the Maxtaloya trachyandesites (Qta4) constituting the rim-walls of Xalapasco craters, (iii) LH4 from San Antonio-Las Chapas lavas (Qta3) outcropping in the Los Humeros town, (iv) LH5-2 from mafic lavas (Qb1) outcropping west to Los Humeros town, (v) LH5-1 from

Chicomiapa-Los Parajes felsic lavas (Qt2) outcropping in the north-western part of Los Potreros caldera, (vi) LH6-1 from El Pajaro unit (Qt1) outcropping in the north-western part of Los Potreros caldera. In addition to these units, we also collected three more samples (LH13, LH26-1 and LH26-2) from lavas and domes of intermediate compositions, outcropping (Fig. 2b-c) in the central part of Los Potreros caldera between Xalapasco crater and Los Humeros town, and not reported on the published geological map.

The samples were investigated through: i) an integration of polarized-light microscopy (PLM) and electron microprobe analyses (EMPA) for the definition of magmatic fabrics, textures, mineral assemblages and mineral chemistry; and ii) ion coupled plasma – optical emission (ICP-OE) and X-ray fluorescence (XRF) analyses to determine the whole-rock major element compositions.

Analytical protocols are described in the Appendix A. In the following, mineral abbreviations are after Whitney and Evans (2010).

4.MAJOR ELEMENT BULK COMPOSITION

Studied samples (Fig. 3a) show a continuous series from mafic to felsic compositions, with SiO_2 ranging 46.5-67.6 wt%, and $Na_2O + K_2O$ ranging 3.4-9.2 wt% (with $K_2O/Na_2O < 1$) (Table 1). LHPCS mafic rocks ($SiO_2<$ 50 wt%; 3 samples) show composition with SiO_2 46.5-49.4 wt%, Al_2O_3 16.2-17.1 wt%, MgO: 8.0-8.4 wt%, CaO: 9.8-10.7 wt%, with Mg# (molar $MgO/[MgO+FeO_{tot}]$) = 60-61 and Na_2O+K_2O ranging 3.4-3.5 wt%. LHPCS intermediate rocks ($50<SiO_2<63$ wt%; 8 samples) contain 54.4-62.1 wt% SiO_2, with Al_2O_3 15.7-20.7 wt%, Na_2O+K_2O 5.3-7.1 wt%, MgO 2.2-3.6 wt% (Mg# 43-51), and low CaO 4.6-8.5 wt%. LHPCS felsic rocks ($SiO_2>63$ wt%; 2 samples) show SiO_2 ranging 64.9-67.6 wt%, associated with Al_2O_3 15.5-15.8 wt%, MgO 0.7-1.2 wt% (Mg#: 26-34), CaO 2.1-2.8 wt%, and Na_2O+K_2O 8.2-9.2 wt%.

On the total alkali versus silica (TAS) diagram (Le Maitre et al., 2002) LHPCS lavas span from basalts to basaltic trachyandesites, trachyandesites and trachytes (Fig. 3b). Los Humeros mafic rocks fall in the "Basalt" field and, according to Bellieni et al. (1983), Le Maitre et al. (2002) and Giordano et al. (2012), can be classified as alkali-basalts. The high TiO_2 contents (1.34-1.5 wt%), together with MgO <12 wt% and low Al_2O_3/TiO_2 values (average value 11.5) exclude the LH mafic rocks as high-Mg melts (picrites) or komatiites (e.g., Redman and Keays, 1985; Arndt and Jenner, 1986; Le Maitre et al., 2002; Gao and Zhou, 2013; Azizi et al., 2018a, 2018b).

Intermediate products fall in the "Basaltic trachyandesites" and "Trachyandesites" fields; these rocks showing intermediate composition will be referred hereafter as "trachyandesites".

The Los Humeros felsic (i.e., SiO_2 >63 wt%) lava samples belonging to the post-caldera stage (i) fall in the "Trachyte" fields, (ii) show potassic signature and (iii) are characterized by Agpaitic Index (molecular ratio $[(Na_2O+K_2O)/Al_2O_3]$) values < 1 (range: 0.7-0.8) thus excluding a peralkaline character of these evolved melts. Selected Harker diagrams for major elements are presented in Figure 3, using SiO_2 wt% as

differentiation index. Negative correlations are observed for CaO (Fig. 3c) and Mg# (Fig. 3d), whereas positive correlations are observed for Na_2O (Fig. 3c).

5.PETROGRAPHY

5.1 Basalts

LHPCS basalts show vesicle-rich (up to 35 vol%) highly-porphyritic (phenocrysts up to 50 vol%) textures (Fig. 4a-d). Studied basalts are invariably free of lithics and a fluidal fabric is defined by the alignment of plagioclase laths in the groundmass. Based on the presence of clinopyroxene (Cpx) in the mineral assemblage, basalts can be further subdivided into: (i) Cpx-free basalt of extra-caldera Texcal lava flow (LH18); and (ii) Cpx-bearing basalts of intra-caldera lavas at western Los Potreros and at Xalapasco crater (LH5-2 and LH27-1, respectively).

Cpx-free basalt (LH18) contains euhedral to subhedral olivine (ca. 20 vol%) and plagioclase (ca. 25-30 vol%) phenocrysts in a holocrystalline groundmass consisting of thin platy plagioclase, dendritic to spinifex olivine and opaque oxides (Fig. 4a, b). Olivine and plagioclase phenocrysts are generally slightly chemically zoned (see below) with a typical core-rim texture (Fig. 4a, b). Occasionally, major phenocrysts of olivine (up to 2.5 mm in size) with Cr-spinel inclusion are observed (Fig. 4a). It is worth notice that no pyroxenes are observed in this basalt.

Cpx-bearing intra-caldera basalts (LH5-2, LH27-1) shows euhedral to subhedral plagioclase (ca. 25 vol%), olivine (ca. 10-15 vol%), yellow to colorless clinopyroxene (ca. 10-15 vol%) and rare anorthoclase (< 2 vol%) phenocrysts (Fig. 4c) in a holocrystalline groundmass (Fig. 4d) made of (in order of microlites abundance) elongated platy plagioclase, olivine, colorless to green clinopyroxene, opaque oxides and rare alkali-feldspar. All phenocrysts show oscillatory growth zoning with distinct core-rim structures (Fig. 4c, d). Large phenocrysts of olivine (up to 1.5 mm in size) and plagioclase (up to 3 mm in length) are commonly observed. Vesicle size is up to 5mm in diameter.

5.2 Trachyandesites

LHPCS intermediate volcanic products show low- to medium-porphyritic textures (phenocrysts ranging 10-40 vol%), with a general fluidal fabric as indicated by orientation of plagioclase and clinopyroxene laths in the groundmass (Fig. 4e, f). Intermediate products vary from poorly vesiculated (< 10 vol% in LH13) to vesicle-rich (ca. 30 vol% in LH4) lavas. In the highest vesiculated sample (LH4), size of vesicles (3-5 mm in diameter) is comparable to those of intra-caldera basalts (LH5-2, LH27-1). Based on the presence of orthopyroxene (Opx) in the mineral assemblage, rocks of intermediate compositions can be further subdivided into: (i) Opx-free (LH21, LH15); and (ii) Opx-bearing (LH4, LH13, LH17, LH26-1, LH26-2, LH27-2) trachyandesites.

Opx-free trachyandesites shows euhedral to subhedral plagioclase (ca. 15-20 vol%), yellow to colorless clinopyroxene (ca. 10-20 vol%), alkali-feldspars (ca. 10-15 vol%) and olivine (ca. 10 vol%) phenocrysts, in holocrystalline microcrystalline groundmass composed of elongated platy plagioclase, colorless clinopyroxene, olvine, alkali-feldspar and opaque oxides, in order of microlites abundance.

Apart from the olivine-free LH27-2 sample, Opx-bearing trachyandesites are generally characterized by euhedral to subhedral plagioclase (ca. 15-20 vol%), clinopyroxene (ca. 10-20 vol%), colorless orthopyroxene (ca. 10-20 vol%), alkali-feldspars (ca. 10-15 vol%) and olivine (< 10 vol%) phenocrysts in a holocrystalline to hypohyaline microcrystalline groundmass made of feldspar (plagioclase and alkali-feldspars) microlites, pyroxene (clinopyroxene and orthopyroxene) microlites, olivine microlites, opaque minerals and glass (Fig. 4f).

Most of phenocrysts observed in these intermediate rocks present oscillatory growth zoning with core-rim structures (Fig. 4e); however, unzoned Cpx phenocrysts are also observed. Major phenocrysts of Cpx (up to 2 mm in size) and Pl (up to 2 mm in length) are commonly observed in all studied trachyandesites. Plagioclase phenocrysts with inherited cores are reported. Rare large phenocrysts of olivine (1.5-2.0 mm in size), presenting disequilibrium textures at rim and characterized by spinel inclusion, are reported in LH26-1 sample.

5.3 Trachytes

LHPCS trachytes show phyric textures, with low porphyritic index (phenocrysts ranging 10-25 vol%), and fluidal fabrics as shown by iso-orientation of plagioclase, alkali-feldspars and clinopyroxene laths in the groundmass (Fig. 4g, h). They range from vesicle-poor (< 5 vol%) to vesicle-free textures, with size of vesicles never exceeding 0.05 mm in diameter. The two analyzed trachytic samples (LH5-1 and LH6) are both characterized by the presence of orthopyroxene; however, the two mineral assemblages differ substantially.

The low-SiO_2 (64.93 wt%) LH5-1 trachyte is characterized by euhedral to subhedral plagioclase (ca. 10-15 vol%), clinopyroxene (ca. 10 vol%), orthopyroxene (ca. 10 vol%), olivine (ca. 5-10 vol%) and sanidine (< 10 vol%) phenocrysts in a hypohyaline microcrystalline groundmass made of (in order of abundance of microlites) sanidine, rare plagioclase, orthopyroxene, clinopyroxene, olivine, opaque minerals and glass. Phenocrysts are generally unzoned, however rare major plagioclase (up to 1.5 mm in length) and clinopyroxene (up to 1.0 mm in length) phenocrysts are characterized by inherited cores and inclusions of olivine + magnetite, respectively. The high SiO_2 (67.58 wt%) LH6 trachyte is made up of sanidine (ca. 10 vol%), plagioclase (ca. 5-10 vol%) and orthopyroxene (ca. 10 vol%) phenocrystals in a fine grained trachytic mesostasis. Only the mafic phenocrysts show core-rim textures. Dimension of phenocrysts are comparable to those of LH5-1 trachyte.

Solid Earth Discuss., https://doi.org/10.5194/se-2019-86
Manuscript under review for journal Solid Earth
Discussion started: 22 May 2019

6.MINERAL CHEMISTRY

Mineral compositions as obtained from electron microprobe analyses and mineral formulae for mineral assemblages of LHPCS lavas are presented in Supplementary Tables 1, 2, 3, 4 and 5 (for feldspar, clinopyroxene, olivine, orthopyroxene and spinel and opaque minerals, respectively).

6.1 Feldspar

In basaltic rocks (Fig. 5a), feldspars are predominantly plagioclase. Phenocrysts show normal core-rim zonation with anorthite-rich (XAn = 43-95%) cores and labradorite (XAn = 42-59%) rims. Orthoclase component (XOr) is always less than 2%. Plagioclase microlites in the groundmass show andesine (XAn = 19-60%) composition, with XOr ranging 1-7%. Alkali-feldspars occur as rare anorthoclase phenocrysts ($Ab_{60}Or_{37}$), and as microlites in groundmass ($Ab_{62-79}Or_{9-35}An_{0-13}$).

Plagioclase from trachyandesites (Fig. 5b) have anorthite-rich (XAn = 47-77%) cores and essentially andesine (XAn = 27-69%) rims. Inherited cores with XAn up to 98% are observed in major phenocrysts. The XOr ranges 1-8%. Plagioclase microlites in groundmass show andesine (XAn = 29-63%) composition with XOr always less than 10%. Alkali-feldspars occur as (i) anorthoclase ($Ab_{59-68}Or_{11-30}$) and sanidine ($Ab_{49-50}Or_{43-48}$) phenocrysts, and (ii) anorthoclase ($Ab_{49-70}Or_{15-38}$) and sanidine ($Ab_{38-48}Or_{47-61}$) microlites in groundmass.

Trachytes (Fig. 5c) show generally unzoned plagioclase phenocrysts with oligoclase-andesine (XAn = 26-45%) composition. Rare labradorite (XAn= 52-70%) inherited cores are reported in the low-silica trachyte LH5-1. The XOr is always less than 8%. Plagioclase microlites in groundmass are rare, with oligoclase ($An_{21-30}Ab_{66-69}Or_{4-10}$) composition. Alkali-feldspars are represented by anorthoclase as phenocrysts ($Ab_{65-66}Or_{20-21}$) and groundmass microlites ($Ab_{64-66}Or_{21-24}$).

6.2 Clinopyroxene

Apart from the LH18 basalt and LH6 trachyte, clinopyroxene, is the most common mafic mineral recognized in studied samples. It occurs generally as single crystals (Fig. 4e), however crystals clots are also reported in trachyandesites. Major clinopyroxene phenocrysts in trachyandesites and trachytes contain inclusions (Fig. 4e, g) of olivine, magnetite and plagioclase.

Polarized light microscopy coupled with BSE images and chemical investigations highlighted the presence of unzoned (Fig. 4g) and zoned (core-rim structure, Fig. 4e) clinopyroxene phenocrysts, with minor or no evidence of resorption/dissolution. The Cpx composition (Fig. 6 a-f) can be grouped in five major categories: (i) cores of zoned phenocrysts in basalts (Cpx1); (ii) cores of zoned phenocrysts in trachyandesites and trachytes (Cpx2); (iii) rims of zoned phenocrysts and unzoned phenocrysts in all studied samples (Cpx3); (iv) microlites in groundmass in all studied samples (Cpx4); and (v) emerald green to greenish euhedral to subhedral microlites in groundmass of intra-caldera basalts (LH5-2, LH27-1) and

thin external rims of major clinopyroxene phenocrysts from a restricted number of trachyandesites (LH15, LH17, LH26-2) (Cpx5).

The Cpx1 shows Mg# of 45-75, Ca 0.78-0.90 apfu, Q+J 1.84-1.94 and J/(J+Q) 0.03-0.06, and it can be classified as Ti-rich augite ($Wo_{41-48}En_{25-42}Fs_{14-32}$).

The Cpx2 shows a Mg# of 59-84, Ca 0.20-0.92 apfu, Q+J 1.77-1.95 and J/(J+Q) 0.01-0.06, and it can be classified as diopside-rich augite ($Wo_{11-48}En_{36-64}Fs_{9-32}$).

The Cpx3 shows Mg#: 20-86, Ca 0.27-0.97 apfu, Q+J 1.57-1.98 and J/(J+Q) 0.01-0.07, and it can be classified as diopside-rich augite ($Wo_{12-49}En_{14-57}Fs_{8-62}$).

The Cpx4 shows Mg# of 31-81, Ca 0.24-0.87 apfu, Q+J 1.87-1.97 and J/(J+Q) 0.01-0.06, corresponding to diopside-rich augite ($Wo_{12-46}En_{18-60}Fs_{11-38}$).

The Cpx5 differs from previous pyroxenes, with a large spread in Mg# ranging 5-73, Ca 0.03-0.83 apfu, Q+J 1.51-2.07 and J/(J+Q) 0.07-0.89. The Cpx5 can be classified as Aegirine-Augite (Na< 0.3 apfu, XAeg< 0.30; with XAeg= Na apfu if Na < $Fe^{3+\ Tot}$, XAeg= $Fe^{3+\ Tot}$ apfu if Na > Fe^{3+Tot}) to Aegirines (Na= 0.68-0.88 apfu, XAeg= 0.40-0.88). Cpx5 clinopyroxenes are generally Ti-enriched (TiO_2 up to 2.8 wt%, Ti up to 0.08 apfu) and straddle the Q+J=2 line defining the boundary for "normal" pyroxenes (Morimoto, 1989), thus indicating the presence of a $NaR^{2+}_{0.5}Ti^{4+}_{0.5}Si_2O_6$ component (Morimoto, 1988, 1989; Huraiova et al., 2017) (Fig. 6c).

The compositional variation of clinopyroxenes can be summarized in the Na vs. Ti diagram (Fig. 6e-f). Interestingly, Augite (Cpx1, Cpx2, Cpx3 and Cpx4) clinopyroxenes generally show positive correlation and linear distribution characterized by a progressive Ti- and Na-depletion, from Ti-Augite in basalts to DiHd-rich Augite in trachytes. The Cpx5, belonging to Aegirine-Augite and Aegirine, moves away from this trend showing a negative correlation characterized by a progressive enrichment of Na content, with respect to a general Ti-depletion. Aegirine enrichment is diagnostic of ferric iron (Fe3+) content increasing during the magmatic differentiation, whereas the diopside-hedenbergite enrichment testifies increasing of ferrous iron (Fe2+) in magma (e.g. Huraiova et al., 2017).

6.3 Olivine

Olivine is found in all analyzed samples, except for for LH27-2 trachyandesite and LH6 trachyte. It consists of idiomorphic (Fig. 4 a, c) to skeletal (e.g., Donaldson, 1974; Fowler et al., 2002; Faure et al., 2003; Welsch et al., 2013) (Fig. 4b) phenocrysts, and microlites in the groundmass (Fig. 4h). It shows a continuous compositional range (Fig. 7a) from $Fo_{86}Fa_{14}Mtc_0Tep_0$ (phenocryst in LH5-2 basalt) to $Fo_{05}Fa_{91}Mtc_1Tep_3$ (groundmass microlites in LH27-1 basalt). Maximum MnO (up to 1.7 wt%) values are always found in Fe-rich olivine microlites. Low monticellite concentration (CaO always < 1.0 wt%) in Los Humeros sample is typical for magmatic olivine (i.e., Melluso et al., 2014). CaO content positively correlates with the fayalite (FeO) compound (Fig. 5a). Together with the Mg#, the CaO content allows to discriminate olivine

phenocrysts in three coherent compositional clusters: i) phenocrysts from basalts, with Mg#= 79-87 and CaO= 0.21-0.73 wt%, ii) phenocrysts from trachyandesites, with Mg#= 67-80 and CaO= 0.08-0.43 wt%, and iii) phenocrysts from trachytes with Mg#= 58-63 and CaO= 0.16-0.42 wt%. A minor cluster of peridotite Mg-olivine ($Fo_{99}Fa_1$) xenocrysts, characterized by disequilibrium textures, have been identified in LH26-1 trachyandesite lava.

6.4 Orthopyroxene

Orthopyroxene occurs in most of the LHPCS trachyandesite (Fig. 4f) and trachyte samples (Fig. 4 g-h). Orthopyroxene phenocrysts show intermediate ($En_{41-83}Fs_{14-55}Wo_{2-10}$) compositions (Fig. 7b), with Mg# of 43-86, Al_2O_3 up to 2.12 wt%, TiO_2 0.08-1.33 wt%, and CaO 1.20-4.72 wt%. Similar compositions ($En_{62-79}Fs_{18-33}Wo_{3-7}$) have been obtained for microlites in groundmass (Fig. 7b) with Mg# of 65-81, Al_2O_3 0.48-1.53 wt%, TiO_2 0.21-0.60 wt% and CaO 1.35-3.49 wt%.

In trachytes, orthopyroxene phenocrysts present Mg# ranging 59-65, with low Al_2O_3 (0.18-0.73 wt%), low TiO_2 (0.11-0.32 wt%) and CaO (0.81-1.88 wt%), corresponding to Fe-rich composition ($En_{56-63}Fs_{34-39}Wo_{2-4}$) with a minor Ca-Cpx substitution (Fig. 7b). Orthopyroxene microlites in groundmass (Fig. 7b) show comparable hypersthene ($En_{46-60}Fs_{35-45}Wo_{3-7}$) composition with Mg# of 50-63, Al_2O_3 0.25-0.82 wt%, TiO_2 0.19-0.31 wt% and CaO 1.32-3.27 wt%.

The compositional variation of orthopyroxyene is summarized in Al^{Tot} vs. Mg# diagram (Fig. 7c). In general, orthopyroxene from trachyandesites is characterized by higher content of Al (apfu) and higher Mg#, whereas those from trachytes are richer in ferrous iron (lower Mg# values) and in manganese (Mn up to 0.04 apfu).

6.5 Spinel and Opaque Minerals

Basalts show a diversified set of opaque minerals. Phenocrysts are characterized by, in order of abundance, the presence of: i) Al-spinel (TiO_2 0.58-1.00 wt%; Mg# 58-71; Cr# 21-30) (with [Cr#= 100 Cr/(Cr+Al)]), ii) Ti-magnetite (TiO_2 1.83-21.58 wt%; MgO 0.06-2.19 wt%; MnO 0.44-0.63 wt%) and ilmenite (MgO up to 2.18 wt%). Groundmass is characterized by the only presence of Fe-Ti oxides as ilmenite (MgO 0.27-1.50 wt%) and Ti-magnetite (MgO 0.18-1.89 wt%). Cr-spinels (TiO_2 3.37-8.55 wt%; Mg# 14-28; Cr# 62-72) are found just as inclusions in larger Mg-rich olivine phenocrysts.

Trachyandesites are characterized by phenocrysts of Ti-magnetite (MgO 0.07-3.84 wt%), ilmenite (MgO 1.11-4.79 wt%) and rare rutile (MgO 0.47 wt%). Groundmass shows a comparable composition with Ti-magnetite (MgO 0.33-3.77 wt%), ilmenite (MgO 0.33-4.79 wt%) and rare rutile (MgO < 0.05 wt%). Comparable to basalts, Cr-spinels (TiO_2 6.09-6.47 wt%; Mg# 19-21; Cr# 65-68) are identified only as inclusions in major Mg-rich phenocrysts.

In Trachytes, Fe-Ti oxides show euhedral to subhedral habit and, based on chemistry, they are ilmenite (MgO 2.06-3.31 wt%) and titanomagnetite (MgO 1.41-5.47 wt%). Phenocrystals and groundmass show same compositions.

7. DISCUSSION

Many different thermobarometry models have been developed since the very early studies of Daubeny (1835), which can be classified as follows: (i) based on mineral-chemistry only (e.g., Lindsley, 1983; Nimis, 1995; Schimdt, 1992; Vidal et al., 2005; Putirka, 2008; Mutch et al., 2016); (ii) based on melt-chemistry (or "liquid"-chemistry) only (e.g., Thornber et al., 2003; Putirka, 2008); and (iii) based on equilibria between mineral phase and coexisting melt (or "liquid") pairs (Holland and Blundy, 1994; Anderson et al., 2008; Putirka, 2008 and references therein). As clarified by Putirka (2008), "liquid" could be the composition of the glass, or the whole rock, or either calculated compositions taken to be representative for the melt at equilibrium with a given mineral phase. Furthermore, as a general rule, Putirka (2008) in his review suggests comparing phenocrysts to the whole rock composition as well as microcrystals/microlites to the glass in groundmass.

In order to define the thermo-baric environmental conditions of the magmatic feeding system of the LHPCS, we integrated thermobarometry models based on olivine (Beattie, 1993; Putirka et al., 2007; Putirka, 2008), orthopyroxene (Putirka, 2008), plagioclase (Putirka, 2005b; Putirka, 2008), alkali-feldspar (Putirka, 2008) and clinopyroxene (Putirka et al., 1996, 2003; Putirka, 2008; Masotta et al., 2013) chemistry and since the paucity/absence of glasses, we assumed the whole rock composition as representative of the original liquid (or nominal melt) in equilibrium with phenocrysts (Putirka, 1997, 2008; Mordick and Glazner, 2006; Aulinas et al., 2010; Dahren et al., 2012; Barker et al., 2015). We are aware that such a procedure put the focus on early steps of the crystallization history, characterized by high melt/crystal ratios. Relatively late melt compositions, related to the solidification of the groundmass, are not present or can simply not be analyzed. Thermobarometric calculations were developed after the application of mineral-melt equilibrium filters and considering pre-eruptive H_2O^{liq} values Plagioclase-liquid thermometry and barometry were calculated using eq. (24a) and eq. (25a), respectively, of Putirka (2008), mainly based on the Ca/Na distribution between melt and Pl. Alkali-feldspar-liquid thermometry was calculated considering the K-Na exchange, applying eq. (24b) in Putirka (2008). Olivine-liquid equilibrium thermometry was calculated integrating the models of Beattie (1993) and Herzberg and O'Hara (2002) with the thermometric eq. (2) in Putirka et al. (2007). Orthopyroxene-liquid thermometry was calculated by Fe-Mg partitioning following the model of Beattie (1993; in the revised form [eq. 28a] in Putirka, 2008). For barometry, based on the Na and Al content in Opx, the model of Wood (1974) in the revised form [eq. 29a] in Putirka (2008) was applied.

Clinopyroxene-liquid thermometry and barometry, for diopside-augite pyroxenes in basalts and trachyandesites (groups Cpx1, Cpx2, Cpx3, Cpx4), were calculated by the application of the Jd-DiHd exchange thermometer (Putirka et al, 1996, 2003) using [eq. 33] in Putirka (2008) and the Al-partitioning barometric model [eq. 32c] in Putirka (2008). Clinopyroxene-liquid thermometry and barometry, for diopside-augite pyroxenes in trachytes (groups Cpx3 and Cpx4), were calculated by the application of the Jd-DiHd exchange thermometer (Putirka et al, 1996, 2003; Putirka, 2008) recalibrated for alkaline differentiated magmas using [eqn. Talk33] and [Eqn. Palk 2012], respectively, in Masotta et al. (2013). Clinopyroxene-liquid thermometry and barometry, for augite-aegirine pyroxenes (Cpx5), were calculated integrating [eq. 33] and [eq. 32c] in Putirka (2008) with equations [Eqn. Talk2012] and [Eqn. Palk 2012] in Masotta et al. (2013). Results of mineral-melt equilibrium tests (Figs. 8, 9, 10), hygrometry calculations (Fig. 10) and geothermometric estimates are presented contextually in supplementary mineral chemistry tables. Summary of the thermobarometry estimates are reported in a Pressure-Temperature diagram (Fig. 11).

7.1 Test for Mineral-Melt Equilibrium

Prerequisite for the application of inverse thermobarometry models based on mineral-melt equilibrium conditions is to test and verify that mineral and the chosen liquid composition represent chemical equilibrium pairs (e.g., Putirka, 2008; Keiding and Sigmarsson, 2012). Petrographic investigations (i.e., polarized light and BSE imaging) and calculation of mineral-liquid partition coefficients were integrated with the aim to select only mineral populations that are in apparent equilibrium with the melt (e.g., Putirka, 2008; Keiding and Sigmarsson, 2012).

The predominant euhedral to subhedral habit of crystals is generally considered an evidence of equilibrium with the surrounding melt (e.g., Keiding and Sigmarsson, 2012). Accordingly, in the first step of our analysis we discarded from the analyzed dataset the the minor cluster of crystals presenting morphological evidence of disequilibrium such as patchy chemical zoning (from BSE images) was also discarded.

Critical for thermo-barometric studies is the use of strongly oscillatory zoned phenocrysts (e.g., Mordick and Glaznier, 2006; Putirka, 2008; Keiding and Sigmarsson, 2012), because the strongly zoned nature implies that core and rim of a grain formed in evolving liquids with progressively different compositions. Considering the absence of glass in most of the analyzed LHPCS samples, we use whole-rock compositions as representative of pristine liquids in equilibrium with early crystallized phenocrysts and microlites.

As second step, mineral-liquid equilibria between liquid and previous selected minerals, were investigated using: (i) the Fe-Mg exchange coefficient, (ii) the An-Ab partitioning coefficient, and (iii) the comparison between observed and predicted normative components of minerals.

The partitioning of Fe-Mg between mineral and liquid is known as Fe-Mg exchange coefficient, or $K_D^{min\text{-}liq}$(Fe-Mg) (defined as $K_D^{min\text{-}liq}$(Fe-Mg) = [$MgO^{liq}FeO^{min}$]/[$MgO^{min}FeO^{liq}$], where *liq* is the liquid composition, *min* is the mineral composition and MgO and FeO are molar fractions; Roeder and Emslie, 1970; Langmuir

and Hanson, 1981; Putirka, 2005a; Putirka, 2008). It is used here to test the equilibrium between mafic minerals (olivine, orthopyroxene and clinopyroxene) and liquid (e.g., Maclennan et al., 2001; Putirka, 2008; Stroncik et al., 2009; Aulinas et al., 2010; Keiding and Sigmarsson, 2012; Melluso et al., 2014; Feng and Zhu, 2018). The $K_D^{min\text{-}liq}$(Fe-Mg) value in Opx is almost independent of P and T, but decreases slightly with the increasing silica content in melt (Putirka, 2008). For a given liquid, we calculated, the ideal Fe-Mg exchange (hereafter iK_D) value using the equation proposed by Putirka (2008): $iK_D^{min\text{-}liq}$(Fe-Mg) = 0.4805-0.3733*Si^{liq}, where Si^{liq} is the cation fraction of SiO_2 in the liquid. The criterion [$K_D^{opx\text{-}liq}$(Fe-Mg)] – [$iK_D^{opx\text{-}liq}$(Fe-Mg)] < 0.10 has been here chosen as additional test in evaluating Opx-melt equilibria.

Due to the slight temperature dependency of Fe-Mg exchange for Cpx-Liq pairs (Putirka, 2008), we calculated $K_D^{min\text{-}liq}$(Fe-Mg) values, based on measured rock and mineral compositions, using (i) equation (17) in Putirka (2008) for Ol and Opx, (ii) temperature-dependent equation (35) in Putirka (2008) for diopsidic-augitic Cpx and iii) Na-dependent equation (35a) in Masotta et al. (2013) is integrated for Cpx-bearing trachytes and Na-aegirine Cpx5. The calculated $K_D^{min\text{-}liq}$(Fe-Mg) are plotted in a Rhodes's diagram (Dungan et al., 1978; Rhodes et al., 1979; Putirka, 2005; Putirka, 2008) to graphically test the equilibrium between Ol (Fig. 8a) or Opx (Fig. 8b) and the Liq. Furthermore, the Rhodes's diagram is useful to recognize processes such as: (i) presence of xenocrystals and antecrystals; (ii) late or groundmass crystallization; (iii) crystal removal (decrease of $Mg\#^{liq}$ only); and (iv) closed system crystallization (decrease of $Mg\#^{min}$ only) by deviations of the measured compositions from the expected ones (Rhodes et al., 1979; Putirka, 2008; Melluso et al., 2014).

The calculation of $K_D^{cpx\text{-}liq}$(Fe-Mg) does not consider variations of Ca and Al contents in Cpx (Rhodes et al., 1979; Putirka, 1999, 2005b, 2008). Therefore, a further equilibrium test was achieved through the comparison of analysed Cpx compositions (as expressed by the components EnFs, DiHd and Ca-Ts, where Ca-Ts stays for Ca-Tschermak) with component contents predicted from melt composition (e.g., Putirka, 2008; Mollo et al., 2010; Jeffery et al., 2013; Barker et al., 2015; Ellis et al., 2017). Normative components of Cpx were calculated following the scheme proposed in Putirka et al., (1996) and Putirka (2008); whereas calculation of Cpx components based on melt composition was performed using equations (eq 3.1a) for DiHd, (eq 3.2) for EnFs and (eq 3.4) for Ca-Ts in Putirka (1999). A graphical presentation (e.g., Jeffery et al., 2013; Barker et al., 2015) of this test is shown in Figure 9.

The partitioning of An-Ab between mineral and liquid is known as An-Ab exchange coefficient, or $K_D^{pl\text{-}liq}$(An-Ab) (defined as $K_D^{pl\text{-}liq}$(An-Ab) = [$XAb^{pl}XAlO_{1.5}^{liq}XCaO^{liq}$]/[$XAn^{pl}XNaO_{0.5}^{liq}XSiO_2^{iq}$], where *liq* is the liquid composition, *pl* is the plagioclase composition and all components are in molar fractions) (Carmichael et al., 1977; Holland and Powell, 1992; Putirka et al., 2007; Putirka, 2008; Lange et al., 2009; Keiding and Sigmarsson, 2012; Jeffery et al., 2013; Barker et al., 2015; Waters and Lange, 2015). Figure 10 presents a comparison of measured composition of plagioclase with the one calculated from the melt composition

with the thermodynamic model eq (31) in Namur et al. (2012). A similar test can be applied for alkali-feldspars (Putirka, 2008).

In summary, we accept: (i) Ol with $K_D^{ol\text{-}liq}$(Fe-Mg)= 0.30 ± 0.06 (Roeder and Emslie, 1970; Putirka, 2005a; Putirka, 2008 and references therein) (Fig. 8a); (ii) Opx with $K_D^{opx\text{-}liq}$(Fe-Mg)= 0.29 ± 0.06 (Putirka, 2008 and references therein) (Fig. 8b) or that display differences of ± 0.05 between the observed (K_D) and the ideal (iK_D) values of the Fe-Mg exchange (Putirka, 2008 and references therein); (iii) Cpx with $K_D^{cpx\text{-}liq}$(Fe-Mg)= 0.28 ± 0.08 (Putirka, 2008) and that verify the one-to-one (± 0.1) relationship between predicted vs. observed normative components (EnFs, DiHd and Ca-Ts) for at least two of the monitored components (Fig. 9); (iv) Pl with $K_D^{pl\text{-}liq}$(An-Ab)= 0.27 ± 0.11 for T > 1050°C and $K_D^{pl\text{-}liq}$(An-Ab)= 0.10 ± 0.05 for T < 1050°C (Putirka, 2008) or that fall within ± 0.1 of the one-to-one relationship between predicted vs observed An components (Fig. 10); and (v) Afs with $K_D^{afs\text{-}liq}$(An-Ab)= 0.27 ± 0.18 (Putirka, 2008). All mineral-liquid pairs exceeding the accepted exchange coefficient values for Ol, Cpx, Opx and Fsp were discarded for thermobarometric analyses.

7.2 Pre-eruptive H_2O^{liq} content estimates

Many thermobarometric models for volcanic system require an initial estimate of the pre-eruptive water concentration (wt%) in melt (H_2O^{liq}), which was determined in this work by using the plagioclase-liquid hygrometer model [eq. 25b] in Putirka (2008). Hygrometry calculations were produced after the application of plagioclase-liquid equilibrium filters. The calculated pre-eruptive H_2O^{liq} wt% values (±1σ standard deviation of the weighted mean) are plotted as isolines in Fig. 10. The hygrometer of Putirka (2008) indicates(Fig. 10): (i) H_2O^{liq} negative values in basalts, from -0.20 to -0.40 wt%, with a weighted mean of -0.37 ± 0.20 wt% (MSWD= 0.0026; n= 95); (ii) trachyandesites pre-eruptive water content in the range H_2O^{liq}: 0 – 1.40 wt% (weighted mean of 0.57 ± 0.12 wt%, MSWD= 0.12, n= 246); and (iii) trachytes with the highest water concentration (H_2O^{liq}: 1.40 – 1.90 wt%; weighted mean of 1.46 ± 0.32 wt%, MSWD= 0.059, n= 37). Following the approach of Keiding and Sigmarsson (2012), negative values in basalts are interpreted as anhydrous melt compositions.

Application of plagioclase-liquid hygrometer model (Putirka, 2008) define anhydrous environment for pressure-temperature calculations in basalts. Whereas hydrous conditions are required for evolved LHPCS melts and in particular for trachytic lavas, where the impact of 1 wt% H_2O is expected to generate a temperature decrease of ca. -40 °C and a pressure increase of ca. + 1.0 kbar in geothermometers and geobarometers, respectively (Putirka, 2008; Keiding and Sigmarsson, 2012).

On contrary, existing studies (e.g., Kushiro, 1969; Sisson and Grove; 1993; Yang et al., 1996; Putirka, 2005a, 2005b, 2008; Kelley and Barton, 2008; Keiding and Sigmarsson, 2012) demonstrated a negligible effect of water for basaltic and intermediate melts with H_2O^{liq} 0 – 1 wt%.

Solid Earth Discuss., https://doi.org/10.5194/se-2019-86
Manuscript under review for journal Solid Earth
Discussion started: 22 May 2019

565 **7.3 Thermobarometry Results**

566 ***7.3.1 Basalts***

567 When applied to phenocryst cores, the Pl-liq thermobarometry (Fig. 11) show that all basaltic materials
568 have magmatic anhydrous T in the range 1230-1266 °C (weighted mean of 1250 ± 5 °C, ±1σ standard
569 deviation of the weighted mean, MSWD= 0.112, n= 95). Pressure estimates are in the range 6.5-8.7 kbar
570 (weighted mean of 7.9 ± 1.1 kbar, ±1σ standard deviation of the weighted mean, MSWD= 0.024, n= 28) for
571 LH18 Ol-basalts, and 7.2-10.3 kbar (weighted mean of 9.2 ± 0.7 kbar (±1σ), MSWD= 0.064, n= 67) for LH5.2
572 and LH27.1 Ol-Cpx-basalt. Olivine-melt equilibrium (Fig. 11), for the olivine compositional range of Fo 80-
573 85%, yields T window of 1240-1297 ± 27 °C (±1σ), consistent with the results obtained with Pl-liq
574 thermometry. The Cpx-thermobarometry (Fig. 11), for both Cpx1 (phenocryst cores) and Cpx3 (phenocryst
575 rims and unzoned phenocrysts), provides temperature of 1006-1209 °C (weighted mean of 1124 ± 12 °C
576 (±1σ), MSWD= 3.4, n= 82). , for P in the range 3.1-11.5 kbar (weighted mean of 7.6 ± 0.8 kbar (±1σ),
577 MSWD= 2.7, n= 36) for Cpx1, and 2.5-7.7 kbar (weighted mean of 4.0 ± 0.8 kbar (±1σ), MSWD= 0.63, n= 14)
578 for Cpx3. Thermobaric estimates for Cpx4 (microlites in groundmass) indicate shallow conditions (0.3 – 3.0;
579 weighted mean of 1.6 ± 1.2 kbar (±1σ), MSWD= 0.38, n= 6) for temperatures (1006-1123 °C; weighted
580 mean of 1060 ± 54 °C (±1σ), MSWD= 2.9, n= 6) comparable to those obtained for Cpx1 and Cpx3. Higher
581 temperature estimates (1067-1221 °C; weighted mean of 1157 ± 53 °C (±1σ), MSWD= 2.4, n= 7) at low-
582 pressure (0.4-4.7; weighted mean of 2.9 ± 1.1 kbar (±1σ), MSWD= 0.83, n= 7) are instead obtained for a
583 limited number of Cpx5 (aegirine-rich) compositions.
584
585 ***7.3.2 Trachyandesites***
586 Based on the Opx- presence/absence criterion, two populations of trachyandesites have been
587 discriminated in this study.
588 Opx-free trachyandesites LH15 and LH21-2 (El Limón and Sarabia lava flows, respectively) are characterized
589 by i) plagioclase phenocryst cores crystallized at T of 1190-1263 °C (weighted mean of 1248 ± 7 °C (±1σ),
590 MSWD= 1.09, n= 39) and P of 4.8-9.4 kbar (weighted mean of 7.7 ± 0.9 kbar (±1σ), MSWD= 0.14, n= 39); ii)
591 comparable temperature (1193-1263 °C; weighted mean of 1227 ± 37 °C (±1σ), MSWD= 2.3, n= 6) and
592 pressure (6.7-9.6 kbar, mean value of 7.8 ± 2.4 kbar (±1σ), MSWD= 0.101, n= 6) obtained for rare
593 phenocryst rims and microlites at equilibrium; iii) olivine-melt equilibrium (with Fo: 75-80%) showing a T
594 window of 1030-1055 ± 27 °C (±1σ); iv) rare Cpx2 (clinopyroxene phenocryst cores) showing equilibrium
595 with melt and yielding T 1061-1239 °C (weighted mean of 1116 ± 29 °C (±1σ), MSWD= 2.3, n= 12) and P ca.
596 2.9 -8.3 kbar (weighted mean of 5.2 ± 1.2 kbar (±1σ), MSWD= 1.5, n= 12); v) Cpx3 (rims of and unzoned
597 phenocrysts) showing equilibrium with melt and yielding thermobarometric results (T 938-1139 °C, with
598 weighted mean of 1074 ± 15 °C (±1σ), MSWD= 1.9, n= 32; and P 1.0-4.4 kbar with weighted mean of 2.8 ±

0.5 kbar (±1σ), MSWD= 0.22, n= 32); vi) Cpx4 (groundmass microcrystals) compositions indicating, with respect to Cpx3, comparable temperatures (1026-1127 °C, with weighted mean of 1059 ± 16 °C (±1σ), MSWD= 0.71, n= 14) at lower pressure conditions (0.3 – 3.6 kbar with weighted mean of 1.4 ± 0.8 kbar (±1σ), MSWD= 0.35, n= 14). The unique Cpx5-liquid pair at equilibrium yielded P-T conditions of 5.6 ± 1.5 kbar and 1122 ± 30 °C.

Thermobarometric estimates (Fig. 11) for Opx-bearing trachyandesites (LH4, LH13, LH17; LH26-1; LH26-2; LH27-2) show overlapping P-T conditions for plagioclase populations with: i) phenocryst cores crystallizing at T: 1145-1228 °C (weighted mean of 1187 ± 4 °C (±1σ), MSWD= 1.17, n= 166) and P: 4.1-7.7 kbar (weighted mean of 5.8 ± 0.5 kbar (±1σ), MSWD= 0.059, n= 166), and ii) phenocryst rims and microcrystals forming at T: 1140-1224 °C (weighted mean of 1168 ± 8 °C (±1σ), MSWD= 0.90, n= 35) and P: 4.4-8.5 kbar (weighted mean of 6.4 ± 1.0 kbar (±1σ), MSWD= 0.14, n= 35). Lower temperatures (1050-1090 ± 27 °C (±1σ)) are obtained using olivine (Fo 70-80%) – liquid equilibrium model.

Thermobarometers applied to pyroxenes indicate: i) Cpx2 (phenocryst cores) crystallizing at T: 979-1204 °C (weighted mean of 1060 ± 8 °C (±1σ), MSWD= 1.7, n= 106) and P: 3.4 -11.65 kbar (weighted mean of 7.0 ± 0.3 kbar (±1σ), MSWD= 0.91, n= 106), ii) Cpx3 crystallizing at T: 958-1106 °C (weighted mean of 1026 ± 6 °C (±1σ), MSWD= 1.3, n= 147) and P: 1.2 -6.9 kbar (weighted mean of 4.3 ± 0.2 kbar (±1σ), MSWD= 0.72, n= 147), iii) rare Cpx4 showing general equilibrium with melt and forming at P-T conditions of : 920-1123 °C (weighted mean of 1020 ± 21 °C (±1σ), MSWD= 2.7, n= 24) and P: 0.1-3.4 kbar (weighted mean of 1.8 ± 0.6 kbar (±1σ), MSWD= 0.56, n= 24), and iv) Opx yielding crystallization conditions, for both phenocrysts and microlites, of T 1048-1123 °C (weighted mean of 1078 ± 5 °C (±1σ), MSWD= 0.24, n= 129) and P: 0 -2.8 kbar (weighted mean of 1.1 ± 0.6 kbar (±1σ), MSWD= 0.057, n= 84). To note the comparable thermometric estimates (Fig. 11) calculated for mafic phases (Ol, Cpx and Opx) whereas only orthopyroxene (Opx) can be considered a tracer of magma stagnations at shallow depth since the invariably lower pressure values obtained by Opx-liquid barometer.

7.3.3 Trachytes

Magmatic P-T conditions (Fig. 11) of trachytes (LH5.1 and LH6) melts are defined by: i) plagioclase crystallization at T: 1050-1094 °C (weighted mean of 1069 ± 6 °C (±1σ), MSWD= 0.39, n= 37) and P: 4.7-9.0 kbar (weighted mean of 6.5 ± 1.0 kbar (±1σ), MSWD= 0.20, n= 37), ii) olivine (Fo55-65%) – liquid regression indicating olivine crystallization at 900-920 ± 27 °C (±1σ), iii) clinopyroxenes crystallization, both phenocrysts (Cpx3) and groundmass(Cpx4), at temperature of ca. 955 °C (weighted mean of 956 ± 14 °C (±1σ), MSWD= 0.00056, n= 17) and very shallow-depth conditions (P weighted means of 2.3 ± 0.9 kbar (±1σ), MSWD= 0.047, n= 10 and 1.6 ± 1.1 kbar (±1σ), MSWD= 0.04, n= 7; for Cpx3 and Cpx4, respectively). Shallow-depth conditions are obtained also for orthopyroxene crystallization with temperature in the range

960-1006 °C (weighted mean of 990 ± 7 °C (±1σ), MSWD= 0.28, n= 49) and P: 0.2-3.6 kbar (weighted mean of 1.6 ± 0.9 kbar (±1σ), MSWD= 0.101, n= 35). Alkali-feldspar-liquid thermometer produced temperature always < 500°C, here interpreted as a subsolidus equilibration of groundmass after eruption. Interesting to note that P-T conditions of plagioclase crystallization are comparable to those obtained for trachyandesitic rocks.

7.4 Magma evolution beneath Los Humeros

The conceptual model of the present-day LHPCS magmatic plumbing system beneath the Los Humeros caldera is presented in Fig. 12. Based on textural observations, mineral chemistry and thermobaric estimates the early HT (1230-1270 °C) stage of LHPCS magma evolution is represented by high-anorthite plagioclase phenocrysts and Mg-rich olivine (XFo= 80-85%) crystallizing in the deep (ca. 8 kbar) basaltic reservoir. Where these magmas erupted directly, they formed Ol-basalt lava flows such as Texcal Lava flow (LH18). This scenario is confirmed by the presence, in LH18 sample, of olivine with spinifex, dendritic and skeletal textures, interpreted as supercooling mineral texture largely resulting from rapid olivine-supersaturate magma rise from deeper level during the eruption (e.g., Donaldson, 1974; Nakagawa et al., 1998; Fowler et al., 2002; Dahren et al., 2012; Welsch et al., 2013). Permanence of Ol-basaltic melts in the deep reservoir, with a decrease in temperature of ca. 100 °C, is indicated by (Ti-rich augites) Cpx1-forming at ca. 7-8 Kbar and 1150 °C (mean values). Where these magmas erupted as intra-caldera ol-basalts (LH5-2, LH27-1), they are characterized by the further crystallization of (i) progressively Fe-rich olivine (up to XFo= 17-20%), (ii) Ab-rich plagioclase (XAn= 25-30%), (iii) Cpx3 unzoned phenocrysts and overgrowth on Cpx1-cores, (iv) Cpx5 (Aeg-Aug) Na-clinopyroxenes and (v) Cpx4 microcrystals and microlites. This mineral assemblage describes a near-isothermal magma uprising within a narrow temperature window of ca. 1070-1150 °C. Such crystal-bearing magmas ascend from the deeper reservoir to intermediates and shallower stagnation levels, where different phases would crystallize, before the eruption (e.g., Feng and Zhu, 2018). However, the high-vesicularity observed in all studied basalts, suggests their rapid ascent and therefore a short time to free-up the volatiles (e.g. Costa et al., 2013; Feng and Zhu, 2018).

Crystallization/fractionation of An-rich plagioclase, Fo-rich olivine and Ti-rich augite in the primary basaltic magma produce residual melts of intermediate compositions. These evolved melts can ascend, carrying early-formed phenocrysts (i.e., anorthitic plagioclase antecrystals), to the intermediate reservoir and stall. Within this intermediate vertically-distributed layered storage system in the middle crust, Cpx2 clinopyroxene and all the rest of plagioclase phenocrysts start to crystallize producing progressively evolved residual melts able to migrate upward in the feeding system (e.g., Freundt and Schminke, 1995; Patanè et al., 2003; Klugel et al., 2005; Stroncik et al., 2009; Aulinas et al., 2010; Dahren et al., 2012; Keiding and Sigmarsson, 2012; Scott et al., 2012; Jeffery et al., 2013; Coombs and Gardner, 2001; Barker et al., 2015; Feng and Zhu, 2018).

668 The shallowest magma stagnation level (< 3kbar; mean 1.5 kbar) has been here interpreted as a complex
669 magma plexus constituted by a system of small magma volumes, distributed in locally interconnected
670 pockets and batches where (i) mafic and intermediate magmas shortly stall prior to erupt and (ii) evolved
671 melts reside for a relatively prolonged time, enough to crystallize orthopyroxene and to enabling the
672 escape of part of the exsolved volatiles (e.g., Feng and Zhu, 2018; Clarke et al., 2007), as suggested by
673 poor-vesicle textures observed in Opx-trachyte samples (LH5-1, LH6-1).
674 Compositional reverse zoning associated with sieve textures and dissolution (lobate and embayed rims)
675 features in phenocrysts are widely considered indicators of both magma mixing and magma replenishment
676 processes (e.g., Wright and Fiske, 1972; Duda and Schminkcke, 1985; Clague et al., 1995; Yang et al., 1999;
677 Klugel et al., 2000; Zhu and Ogasawara, 2004; Stroncik et al., 2009; Ubide et al., 2014; Viccaro et al., 2015;
678 Gernon et al., 2016; Feng and Zhu, 2018). Almost all investigated samples, from basalts to trachytes,
679 contain mainly normally zoned (Pl+Ol+Cpx) or unzoned (as in case of Cpx3 and Opx) phenocrysts. Rare
680 plagioclase and clinopyroxene with patchy cores (not suitable for thermobarometry) are reported. Since
681 reverse zoning and disequilibrium textures are rarely observed, we suggest that magma mixing and magma
682 replenishment processes occur locally and heterogeneously in the plumbing system (e.g., Cashman et al.,
683 2017 and references therein).
684 This hypothesis is in line with the results obtained from tests for mineral-melt equilibria. Rhodes's diagram
685 (Rhodes et al., 1979; Putirka, 2008) for olivine compositions (Fig. 8a) highlights a progressive decrease in
686 $Mg\#^{liq}$ from basalts to trachytes coupled with general absence of xenocrystals/antecrystals cargo. This
687 behavior is compatible with a complete removal from the melt of previously crystallized Mg-olivine (Roeder
688 and Emslie, 1970; Dungan et al., 1978; Rhodes et al., 1979; Putirka, 2008; Melluso et al., 2014). All melts
689 (from basalts to trachytes) show invariably suites of olivines with maximum forsterite (Fo) contents in
690 equilibrium with the respective whole rocks, and vertical trends consistent with closed-system melt
691 differentiation (Roeder and Emslie, 1970; Rhodes et al., 1979; Putirka, 2008; Melluso et al., 2014). Similar
692 behavior is obtained for orthopyroxene (Fig. 8b), where again Rhodes's test highlights absence of
693 antecrystals, and Opx-suites progressively and normally Fe-enriched from trachyandesites to trachytes.
694 Furthermore, the absence of clinopyroxene clots and overgrowth on orthopyroxene do not support the
695 occurrence of magma mixing/refilling (Laumonier et al., 2014; Neave et al., 2014; Zhang et al., 2015; Feng
696 and Zhu, 2018). Such interpretation is supported by field observations, where the interbedded basaltic
697 andesite and trachydacite fall deposits of the ca. 7 ka Cuicuiltic Member show no evidence of magma-
698 mixing (Dávila-Harris and Carrasco-Núñez, 2014).
699 An-Ab partition coefficients (e.g., Putirka, 2008; Jeffery et al., 2013) show a comparable scenario (Fig. 10) in
700 which: (i) basalts are characterized by suites of plagioclases with maximum anorthite (An) contents in
701 equilibrium with the respective whole rocks, and progressive An^{pl} decrease consistent with closed-system
702 differentiation; and (ii) progressive decrease in predicted An^{liq} from basalt to trachyte compatible with

evolved melts production via differentiation. Intermediate and evolved products are characterized by antecrystals (or inherited cores) of anorthitic plagioclase, indicating that melt differentiation processes occurred, involving the coexistence of earlier-crystallized An-rich plagioclase in melts. A similar behavior is observed for clinopyroxene and in particular for Cpx1 and Cpx2 (clinopyroxene cores in basalts and in trachyandesites, respectively) populations. Since these mineral cores (Pl, Cpx1 and Cpx2) generally present normall growth rims (i.e., Ab-rich Pl and Cpx3), we suggest that stagnation levels at both intermediate and shallower depths underwent crystallization in a closed system. Otherwise, features such as: i) diffused reverse zoning, ii) high-temperature crystal-clots, mantling and overgrowth, iii) disequilibrium and dissolution textures (e.g., Stroncik et al., 2009; Cashman et al., 2017; Feng and Zhu, 2018 and references therein), should be widely observed, but this is not the case in the LHPCS studied lavas.

7.5 The magma plumbing system

The petrological archive constituted by LHPCS lavas, spanning from alkali-basalts to trachytes, describe the Holocene activity of Los Humeros volcanic complex. Major element bulk compositions of LHPCS lavas are characterized, in Harker diagrams (Fig. 3 b-d), by linear trends comparable to those expected for cogenetic melts and progressive magma differentiation via fractional crystallization (e.g., Giordano et al, 2012). Intra-caldera basalts show assemblages containing Aegirine-rich clinopyroxenes (Fig. 4 c, d), widely considered as one of the most reliable indicator of magma transition to peralkaline conditions (i.e., White et al., 2009; Melluso et al., 2014). However, absence of olivine in the most evolved LHPCS trachyte (LH6) excludes, at this stage, a connection with typical basalt-pantellerite suites where tephroitic-fayalite is commonly found in high-silica rocks (i.e., White et al., 2005; Ronga et al., 2010; Macdonald et al., 2012, Melluso et al., 2014 and references therein).

Results obtained from the application of different and independent thermobarometry models (Fig. 11) confirm the working hypothesis of a complex magmatic plumbing system rather than a single “standard” magma chamber (e.g., Keiding and Sigmarsson, 2012; Cashman and Giordano, 2014; Cashman et al., 2017; Feng and Zhu, 2018) developed beneath the active Los Humeros caldera and feeding the LHPCS volcanism.

With the aim to propose an updated and realistic conceptual model of the present-day main storage zones and magma plumbing system within the crust below Los Humeros caldera, we integrate pressure-temperature estimates acquired in this work, with the existing data related to crustal structure and properties of the study area. The resulted model is shown in Figure 12.

The density of TMVB crust shows a large range between 1800 Kg/m^3 for unconsolidated sediments to about 3000 kg/m^3 for the lower crust and 3300 kg/m^3 for the upper mantle (Dziewonski and Anderson, 1981; Campos-Enríquez and Sánchez-Zamora, 2000; Davies, 2013). A reasonable available up today compilation of crust data for Los Humeros volcanic complex is recovered by the measure N°10 of the Crust 1.0 global model (Dziewonski and Anderson, 1981; Davies, 2013). The measure N°10 (yellow star in Fig. 1) is located

738 within the study area at the southern termination of the Tepeyahualco Lava Flow and describes a crust
739 (Fig. 12) made of five main seismic layers: i) upper sediments (thickness: 1km, density 2110 km/m^3), ii)
740 middle sediments (thickness: 0.5 km, density 2370 km/m^3), iii) upper crust (thickness: 13.58 km, density
741 2740 km/m^3), iv) middle crust (thickness: 15.27 km, density 2830 km/m^3), and v) lower crust (thickness:
742 13.58 km, density 2920 km/m^3). Inferred (seismic) Moho depth is reported at -41.67 km with an upper
743 mantle density of 3310 km/m^3 (Dziewonski and Anderson, 1981; Davies, 2013). Here we use a five-tiered
744 density model, as derived from the Crust 1.0 global model, for the 41.67 Km continental crust beneath Los
745 Humeros caldera, to convert obtained pressure estimates to depths.
746 The thermobarometry models applied to the LHPCS lavas define a broad region of crystallization between 0
747 and ca. 30 km in depth that can be described with a quadrimodal distribution of pressure values (Fig. 12),
748 which allow us to propose a complex polybaric continuous heterogenous multilayered transport and
749 storage magmatic system.
750 A deep-seated anhydrous Ol-basalt reservoir at depths of ca. 28-33 km (7.6-9.2 kbar), at the boundary
751 between lower and middle crust, below the caldera is recorded by (a) An-rich plagioclase cores (XAn = 50-
752 70 %), and (b) Ti-rich augitic clinopyroxene Cpx1 cores (Mg# up to 75, TiO_2 up to 4.57 wt%) of Cpx1.
753 Overlapping the calculated anhydrous temperature values from plagioclase-liquid, Cpx1 clinopyroxene-
754 liquid and olivine-liquid pairs provide a total range of ca. 1000 – 1300 °C for this mafic reservoir. Highest
755 anhydrous temperature values are achieved for Cpx-free Ol-basalt Texcal lava flow (LH18) where the
756 convergence of plagioclase-liquid thermobarometry and olivine-liquid thermometry models indicate
757 conditions of ca. 1230-1270°C at ca. 8 kbar. Lower anhydrous temperatures of ca. 1000-1210 °C, are
758 obtained at a comparable average pressure value of 7.6 kbar for Cpx-bearing intra caldera Ol-basalts (LH5-
759 2; LH 27-1). These results are in agreement with existing literature on the near-liquidus melting behavior of
760 high-Al basaltic magmas (Mg# ca. 60-70 and Al_2O_3: 17-19 wt%) under dry conditions (e.g., Thompson, 1974;
761 Grove et al., 1982; Crawford et al., 1987; Bartels et al., 1991; Grove, 2000). At 1250-1300 °C and ca. 10 kbar
762 (Point *A* in Fig. 11) the basaltic melt is in equilibrium with a mantle peridotite mineral assemblage of olivine
763 + clinopyroxene (Kushiro and Yoder, 1966; Presnall et al., 1978; Grove et al., 1982; Fuji and Scarfe, 1985;
764 Takahashi, 1986; Fallon and Green, 1987; Bartels et al., 1991; Sisson and Layne, 1993; Wagner et al., 1995;
765 Grove et al., 1997; Grove, 2000; Kinzler et al., 2000). Following the models proposed by Thompson (1974),
766 Bartels et al. (1991) and Grove (2000), a temperature decrease would lead primary melts to pass the “dry
767 basaltic liquidus” and start the crystallization of Ol+Pl (higher temperatures) or Ol+Cpx+Pl (lower
768 temperatures) assemblages (see stability fields in Fig. 11). Given the ubiquitous presence in all LHPCS
769 basalts of well-developed euhedral to subhedral olivine crystals (both phenocrystals and microlites) at
770 equilibrium with anorthitic plagioclase, it is possible to exclude that crystallization history started at depth >
771 ca. 10-12 kbar where olivine is not a stable phase and the primary assemblage would be characterized only

by Cpx+Pl+Sp in equilibrium with melt (Kushiro and Yoder, 1966; Thompson, 1974; Presnall et al., 1978; Bartels et al., 1991; Grove, 2000).

A second magma transport and storage systems can be recognized at depths of 15-30 km (ca. 4.5 – 7.8 kbar), in continuity with the deeper basaltic reservoir and distributed along the whole middle crust thickness, as recorded by the wide range of pressure estimates obtained from plagioclase (XAn= 40-70%) and Cpx2 clinopyroxene cores (Mg#: 59-84; TiO_2 mean value 0.99 wt%). Thermometry models based on plagioclase, Cpx2 clinopyroxene and olivine show convergence for hydrous temperature values in the range of 979 – 1263 °C. Thermobarometry models, together with textures and petrographic relations in all analyzed trachyandesite and trachyte samples suggest that all plagioclase, all Cpx2 clinopyroxene phenocrysts, and part of microlites, grew in this second storage system. In particular, it is possible to observe two main crystallization temperature conditions: (a) at ca. 1190°C (weighted mean value, MSWD= 2.2, n= 205) plagioclase phenocrysts crystallization in trachyandesite melts is observed, whereas (b) at the lower temperature of ca. 1070 °C (weighted mean value, MSWD= 1.7, n= 155) is reported the crystallization of all olivine, all Cpx2 phenocrysts, and plagioclase phenocryst in trachytes. We interpret the common Pl+Cpx2 phenocryst-forming barometric conditions as evidence of a growth-dominated regime within this second magma storage zone (e.g., Barclay et al., 1998; Humphreys et al., 2006; Scott et al., 2012), whereas the smaller crystals (microcrystals and microlites) represent the nucleation-dominated regime (Scott et al., 2012) that can be associated with ascent-related decompression of melts at shallower levels (e.g., Cashman, 1992; Cashman and Blundy, 2000; Humphreys et al., 2009).

The third melt storage zone occurs at shallower depths of ca. 10-15 km, possibly corresponding to the transition between middle- and upper-crust, as indicated by convergence of barometric estimates (weighted mean value of 3.9± 0.2 kbar (±1σ), MSWD= 0.80, n= 203; P ranging ca. 1-7 kbar) obtained from Cpx3 clinopyroxene (i.e., unzoned phenocrysts and overgrowth/rims around earlier formed Cpx1- and Cpx2-cores) population. Cpx3 clinopyroxene-liquid thermometry model indicates, for this third storage zone a mean temperature of 1040 °C (weighted mean value, MSWD= 2.6, n= 203; T ranging ca. 940-1210 °C) comparable to those calculated for Ol+Cpx2 assemblages in the previous described second and deeper stagnation system. The obtained pressure estimates for the second and the third storage systems are compatible with multiple magma storage pockets, in which melts of comparable compositions ascend slowly enough for phenocrysts to form (e.g. Scott et al., 2012), and start cooling before the final ascent to shallower conditions (e.g., Dahren et al., 2012; Chadwick et al., 2013; Gardner et al., 2013; Jeffery et al., 2013; Preece et al., 2013; Troll et al., 2013). Taking into account the textures and the chemistry of Cpx3 clinopyroxene phenocrysts, the obtained thermobarometric estimates could be interpreted as the pressure-temperature environment of last major levels of magma stagnation and fractionation (Putirka, 1997; Klugel et al., 2005; Galipp et al., 2006; Stroncik et al., 2009).

The fourth shallowest storage zone located at depths of ca. 3-7 km (weighted mean value of 1.5± 0.2 kbar (±1σ), MSWD= 0.24, n= 177; P ranging ca. 0.1-4.5 kbar), is required to explain the presence of i) Cpx4 clinopyroxene (microcrystals and microlites) in all LHPCS lavas, ii) Aeg-rich Cpx5 clinopyroxene in basalts, and iii) Fe-olivine (Fo = 55-65%) and orthopyroxene in Opx-bearing evolved LHPCS lavas. Magmas in this shallow storage system show a wide range of temperature values calculated for hydrous melts: a) ca. 1060 °C (weighted mean value, MSWD= 2.4, n= 7) for Aeg-rich Cpx5 crystallization in basalts, b) ca. 1070 °C (weighted mean value, MSWD= 1.09, n= 168) for Cpx4 and Opx crystallization in trachyandesites, and c) ca. 965 °C (weighted mean value, MSWD= 2.2, n= 78) for olivine, Cpx4 and Opx crystallization in trachytes. Thermobaric estimates obtained for Aeg-rich Cpx5 agree with those calculated for transitional basalts at Pantelleria (White et al., 2009 and references therein), whereas orthopyroxene crystallization conditions overlap with the existing literature for intermediate rocks (e.g., Rutherford et al., 1985; Wallace and Anderson, 2000; Reubi and Nicholls, 2004; Allan et al., 2013; Jeffery et al., 2013). The broad distribution of melt chemistry from basalt to trachyte, together with the obtained thermobaric estimates, define a shallow magma storage environment characterized by progressive accumulation of small locally interconnected magma pockets and batches (e.g., Reubi and Nicholls, 2004; Jeffery et al., 2013) dispersed in the upper crust (<10 km) with a possible magma plexus at a depth of 2-4 km under the caldera (e.g., Armienti et al., 1989; Freundt and Schminke, 1995; Pietruszka and Garcia, 1999; Patanè et al., 2003; Klugel et al., 2005; Stroncik et al., 2009; Dahren et al., 2012; Jeffery et al., 2013; Coombs and Gardner,, 2001, 2004).

7.6 Implications for Los Humeros active geothermal systems

Existing conceptual models for Los Humeros volcanic complex are based on the "Standard Model" (*sensu* Gualda and Ghiorso, 2013). These models mainly refer to the Los Humeros activity phase (the "caldera stage" in Carrasco-Núñez et al., 2018 and references therein) that produced voluminous ignimbrites (in particular the Xaltipan ignimbrite) hypothesizing a single, bowl-shaped, long-lived, melt-dominated huge classical magma chamber of 1000-1500 Km^3 in volume, at depth of 5 to 10 km from the surface (Verma, 1983, 1984, 1985a, 1985b; Verma and Lopez, 1982; Verma et al., 1990; Verma and Andaverde, 1995; Verma et al., 2011; Verma et al. 2013; Carrasco-Núñez et al., 2018).

Thermobarometric estimates obtained in this work, combined with petrographic observations and information from the crustal structure beneath Los Humeros caldera, permit us to propose a different conceptual model, made of a complex polybaric magmatic plumbing system of multiple, more or less interconnected magma transport and storage layers, batches and ponds, feeding the Holocene activity of the Los Humeros volcanic complex.

Our results indicate that magma transport and storage levels, beneath Los Humeros caldera, are distributed across the whole crust from ca. 30 to 3 km (from the lower- to the very upper-crust) with density contrasts between different crustal layers acting as a controlling parameter for ascending or stalling magmas (e.g.,

Dahren et al., 2012). Moreover, it is possible to propose that each of these crust/density boundaries will determine lateral transport and grow of magma stagnation pockets (e.g., Dahren et al., 2012). At depths <5km, magmas (from mafic to felsic) ascending from all the lower storage zones, are stalled once more. The shallowest complex multi-storage system is interpreted as a plexus of scattered, more or less interconnected, ephemeral small-volume batches and pockets of melts, without any defined spatial distribution as ruled out by field-locations of the LHPCS studied lavas eruptive centers.

A shallow storage zone presenting magmas with heterogenous compositions (from mafic to felsic) has been already proposed by Dávila-Harris and Carrasco-Núñez (2014) to explain the eruptive history of the intra-caldera Cuicuiltic Member that was produced by the coeval eruption of compositionally contrasting unmixed magmas. However, a shallow ponding system characterized by heterogeneous composition of magmas involved beneath Los Humeros caldera is not an exceptional case. Examples of shallow heterogeneous reservoirs beneath active volcanic complexes are widely reported (e.g., Nairn et al., 1998; Kratzmann et al., 2009; Sigmarsson et al., 2011; Keiding and Sigmarsson, 2012).

Our results also agree with the work of Creon et al. (2018) where calculated fluid saturation depths derived for melt inclusions in post-caldera lavas indicate different magma-ponding levels within a range of depths between 5 and 13 km, coupled with a possible deeper reservoir/origin (26-32 km) and a final shallow stagnation level (ca. 1.5-3.0 km).

The geothermal activity of a volcanic complex is expected to be the result of stagnation and cooling of magmas in the shallower storage zone (e.g., Gunnarsson and Aradóttir, 2015), where classic conductive models are mainly controlled by age and volume of the magmatic system representing the heat source (Smith and Shaw, 1975; Duffield and Sass, 2003; Gunnarsson and Aradóttir, 2015; Carrasco-Núñez et al., 2018).

The present geothermal activity of LHVC is characterized by a limited NNW-SSE non-homogeneous areal distribution within the Los Potreros nested caldera (e.g., Norini et al., 2015). Based on (i) the young (Upper Pleistocene-Holocene) of most of LHPCS volcanic activity, (ii) the relatively small erupted volumes of LHPCS lavas, in particular of those erupted within the Los Potreros caldera, and (iii) a shallow-crust plexus involving heterogeneous unmixed magmas, as derived by results obtained in this work, we therefore discard the hypothesis of a single, large and voluminous shallow magmatic chamber homogenously distributed beneath the caldera, in favor of a more reliable scenario characterized by a shallow magmatic transient batches of different magmas localized beneath Los Humeros nested caldera. In the light of these results, a revision/update of the heat source feeding the Los Humeros geothermal system is needed to produce correct and up-to-date geothermal potential estimates of the geothermal field and to develop efficient geothermal exploration strategies.

8.CONCLUSIONS

In this study we propose an integrated field-based petrographic-mineralogical approach to unravel the evolution and configuration of the present-day magmatic plumbing system that is feeding the post-Caldera stage activity of Los Humeros volcanic complex. The main results of this study can be summarized as follows.

- A polybaric complex transport and storage system, characterized by multiple magma levels more or less interconnected in time, has been recognized based on application of mineral-melt inverse thermobarometry models.
- A deep mafic reservoir (ca. 30km) is identified by Pl+Ol assemblage in basalts. Intermediate magma storage systems (in the whole middle crust) are described by the progressive evolution of clinopyroxene phenocryst-compositions and a shallow magmatic stagnation system (ca. 1.5kbar, 3-5km) has been defined by crystallization of clinopyroxene microlites, aegirine clinopyroxenes in basalt, and in particular by orthopyroxene formation in most evolved melts. All cpx-bearing lavas are produced by progressive differentiation via polybaric fractional crystallization during magmas ascend through the plumbing system.
- The compositional behavior of the main phases (olivine, plagioclase, clinopyroxene, orthopyroxene), together with their preserved textures, permits to exclude, at this stage, a magmatic feeding system dominated by magma mixing and magma replenishment, in favor of a plumbing system dominated by levels, pockets and batches of melt underwent single charge.
- The thermobarometric results obtained in this work indicate that, unlike previously believed, the present configuration of the plumbing system is vertically extensive across the entire crust with a deeper residence zone for basalts at 8 kbar (ca. 30-33 km) and a complex middle to very upper crust zone (0.5 kbar) where basalts rapidly ascend and stall prior to erupt and where smaller batches of magma differentiate to trachyandesites and trachytes at times interconnected with the lower feeding zone.
- The main outcome for the modeling of the magmatic heat source of the geothermal system is the inadequacy of conservative conceptual models based on the classical melt-dominated, single, voluminous, long-lived magma chamber (i.e., “Standard Model”), in favor of an innovative and more realistic vision of magmatic plumbing systems made of multiple, more or less interconnected magma transport and storage layers within the crust, feeding small (ephemeral) magma pockets at shallow-crust conditions.
- The proposed model for the magmatic plumbing system at LHVC provides a new configuration of the heat source feeding the present geothermal reservoir, and therefore, must be consider it for geothermal exploration purposes.

- Our study demonstrate that petrology represents a consistent method, with respect to geophysics investigations and seismic surveys, able to unravel the anatomy of complex magmatic plumbing system.

Solid Earth Discuss., https://doi.org/10.5194/se-2019-86
Manuscript under review for journal Solid Earth
Discussion started: 22 May 2019

APPENDIX A: Analytical details

A.1 Petrography of volcanic samples

Rock magmatic fabrics, textures and mineral assemblages were studied on polished thin sections, using a Nikon Eclipse 50iPol polarized light microscope (PLM) equipped with Nikon Ds-Fi2 CCD camera (Nikon, Tokyo, Japan) and Nikon Nis-Elements software (Ver4.30.01), at Laboratorio di Microtettonica, Dip. Science, Università Roma Tre (Roma, Italia). Mineral abbreviations follow Whitney and Evans (2010).

A.2 Bulk major element geochemistry

After washing in distilled water, samples were grounded in an agate mill, pre-contaminated with an aliquot of sample. Whole-rock major element concentrations (4 samples) were measured at the Activation Laboratories (Ontario, Canada), through ion coupled plasma (ICP)- optical emission (OE).

Additional samples (9) were analyzed by X-ray fluorescence (XRF) using a ZSX Primus II (Rigaku Co., Japan) at Nagoya University, Japan. Loss on ignition (LOI) was measured from the sample powder weight in a quartz glass beaker in the oven at 950°C for five hours. XRF-analyses were carried out following the procedure presented in Azizi et al., (2015; 2018a; 2018b).

For major elements the uncertainty (1 sigma) is estimated better than 2% for values higher than 5 wt %, and better than 5% in the range 0.1-5 wt %.

A.3 Mineral chemistry

Polished thin sections (13 samples) selected for petrography investigations, were then studied for mineral chemistry and ca. 2400 analyses of mineral phases were obtained with a Cameca SX100 electron microprobe (EMP) at the Institut für Anorganische Chemie, Universität Stuttgart. Operating conditions were 15 kV and 10 to 15 nA, counting times of 20 s both for peak and background. Compositions were determined relative to natural and synthetic standards. Spot sizes were 1-10 µm depending on the phases analyzed. Back Scattered Electron (BSE) imaging was obtained by using the same electron microprobe with operating conditions of 15 kV, 50 nA. Mineral structural formulae of feldspar, olivine and spinel were calculated through the software CalcMin_32 (Brandelik, 2009). Mineral structural formulae of orthopyroxene were calculated following Putirka et al. (1996) and Putirka (2008). Clinopyroxene formula has been calculated following procedures reported in Putirka et al. (1996), Putirka (2008), Masotta et al. (2013). Clinopyroxenes were then classified integrating the Wo-En-Fs scheme (Morimoto, 1989) and J vs. Q scheme (Morimoto, 1988, 1989) with J= 2Na apfu and Q= ($Ca+Mg+Fe^{2+}$) apfu. Aegirine (XAeg) component correction, for Na-rich Cpx (Aegirine-Augite series), followed the scheme (XAeg= Na apfu if Na < $Fe^{3+\ Tot}$, XAeg= $Fe^{3+\ Tot}$ apfu if Na > Fe^{3+Tot}) proposed by Putirka et al. (1996), Putirka (2008) and based on Fe^{2+} - Fe^{3+} correction of Lindsley (1983).

ACKNOWLEDGMENTS

The authors wish to thank the Comisión Federal de Electricidad (CFE, Mexico) for their assistance and support. This paper presents results of the GEMex Project, funded by the European Union's Horizon 2020 programme for Research and Innovation under grant agreement No. 727550 (scientific responsibility Guido Giordano), and by the Mexican Energy Sustainability Fund CONACYT-SENER, Project 2015-04-268074 (WP 4.5, scientific responsibility Gerardo Carrasco-Núñez). More information can be found on the GEMex Website: http://www.gemex-h2020.eu.

Authors would like to thank G. Norini for usefull discussions in the field. Special thanks to Javier Hernández, Jaime Cavazos, Francisco Fernández and Alessandra Pensa for their support in the fieldwork and logistics. The Grant to Department of Science, Roma Tre University (MIUR-Italy Dipartimenti di Eccellenza, ARTICOLO 1, COMMI 314-337 LEGGE 232/2016) is gratefully acknowledged.

Solid Earth Discuss., https://doi.org/10.5194/se-2019-86
Manuscript under review for journal Solid Earth
Discussion started: 22 May 2019

961 **REFERENCES**

962
963 Allan, A. S., Morgan, D. J., Wilson, C. J., and Millet, M. A.: From mush to eruption in centuries: assembly of
964 the super-sized Oruanui magma body. Contrib. Mineral. Petr., 166, 143-164, 2013.
965
966 Anderson, J. L., Barth, A. P., Wooden, J. L., and Mazdab, F.: Thermometers and thermobarometers in
967 granitic systems. Rev. Mineral. Geochem., 69, 121-142, 2008.
968
969 Annen, C.: From plutons to magma chambers: Thermal constraints on the accumulation of eruptible silicic
970 magma in the upper crust. Earth Planet. Sc. Lett., 284, 409-416, 2009.
971
972 Armienti, P., Innocenti, F., Petrini, R., Pompilio, M., and Villari, L.: Petrology and Sr-Nd isotope geochemistry
973 of recent lavas from Mt. Etna: bearing on the volcano feeding system. J. Volcanol. Geoth. Res., 39,
974 315-327, 1989.
975
976 Arndt, N. T., and Jenner, G. A.: Crustally contaminated komatiites and basalts from Kambalda, Western
977 Australia. Chem. Geol., 56, 229-255, 1986.
978
979 Aulinas, M., Gimeno, D., Fernandez-Turiel, J. L., Perez-Torrado, F. J., Rodriguez-Gonzalez, A., and Gasperini,
980 D.: The Plio-Quaternary magmatic feeding system beneath Gran Canaria (Canary Islands, Spain):
981 constraints from thermobarometric studies. J. Geol. Soc. London, 167, 785-801, 2010.
982
983 Azizi, H., Najari, M., Asahara, Y., Catlos, E. J., Shimizu, M., and Yamamoto, K.: U–Pb zircon ages and
984 geochemistry of Kangareh and Taghiabad mafic bodies in northern Sanandaj–Sirjan Zone, Iran:
985 Evidence for intra-oceanic arc and back-arc tectonic regime in Late Jurassic. Tectonophysics, 660,
986 47-64, 2015.
987
988 Azizi, H., Lucci, F., Stern, R. J., Hasannejad, S., and Asahara, Y.: The Late Jurassic Panjeh submarine volcano
989 in the northern Sanandaj-Sirjan Zone, northwest Iran: Mantle plume or active margin? Lithos, 308,
990 364-380, 2018a.
991
992 Azizi, H., Nouri, F., Stern, R. J., Azizi, M., Lucci, F., Asahara, Y., Zarinkoub, M. H., and Chung, S. L.: New
993 evidence for Jurassic continental rifting in the northern Sanandaj Sirjan Zone, western Iran: the
994 Ghalaylan seamount, southwest Ghorveh. Int. Geol. Rev., DOI: 10.1080/00206814.2018.1535913,
995 2018b.
996
997 Bachmann, O., and Bergantz, G.W.: On the origin of crystal-poor rhyolites: extracted from batholithic
998 crystal mushes, J. Petrol., 45, 1565-1582, 2004.
999
1000 Bachmann, O., and Bergantz, G.W.: Rhyolites and their source mushes across tectonic settings, J. Petrol.,
1001 49, 2277-2285, 2008.
1002
1003 Barclay, J., Rutherford, M. J., Carroll, M. R., Murphy, M. D., Devine, J. D., Gardner, J., and Sparks, R. S. J.:
1004 Experimental phase equilibria constraints on pre-eruptive storage conditions of the Soufrière Hills
1005 magma. Geophys. Res. Lett., 25, 3437-3440, 1998.
1006
1007 Barker, A. K., Troll, V. R., Carracedo, J. C., and Nicholls, P. A.: The magma plumbing system for the 1971
1008 Teneguía eruption on La Palma, Canary Islands. Contrib. Mineral. Petr., 170, 54, 2015.
1009
1010 Bartels, K. S., Kinzler, R. J., and Grove, T. L.: High pressure phase relations of primitive high-alumina basalts
1011 from Medicine Lake volcano, northern California. Contrib. Mineral. Petr., 108, 253-270, 1991.
1012

Beattie, P.: Olivine-melt and orthopyroxene-melt equilibria. Contrib. Mineral. Petr., 115, 103-111, 1993.

Bégué, F., Deering, C. D., Gravley, D. M., Kennedy, B. M., Chambefort, I., Gualda, G. A. R., and Bachmann, O.: Extraction, storage and eruption of multiple isolated magma batches in the paired Mamaku and Ohakuri eruption, Taupo Volcanic Zone, New Zealand. J. Petrol., 55, 1653-1684, 2014.

Bellieni, G., Justin Visentin, E., Le Maitre, R. W., Piccirillo, E., and Mand Zanettin, B.: Proposal for a division of the basaltic (B) field of the TAS diagram. IUGS subcommission on the Systematics of Igneous Rocks. Circular no.38, Contribution no.102, 1983.

Brandelik, A.: CALCMIN–an EXCEL™ Visual Basic application for calculating mineral structural formulae from electron microprobe analyses. Comput. Geosci-UK, 35, 1540-1551, 2009.

Campos-Enríquez, J. O., Garduño-Monroy, V. H.: The shallow structure of Los Humeros and Las Derrumbadas geothermal fields, Mexico. Geothermics, 16, 539-554, 1987.

Campos-Enrıquez, J. O., and Sánchez-Zamora, O.: Crustal structure across southern Mexico inferred from gravity data. J. S. Am. Earth Sci., 13, 479-489, 2000.

Carmichael, I. S. E., Nicholls, J., Spera, F. J., Wood, B. J., and Nelson, S. A.: High-temperature properties of silicate liquids: applications to the equilibration and ascent of basic magma. Philos. Tr. R. Soc. S-A, 286, 373-431, 1977.

Carrasco-Núñez, G., and Branney, M.: Progressive assembly of a massive layer of ignimbrite with normal-to-reverse compositional zoning: the Zaragoza ignimbrite of central Mexico. B. Volcanol., 68, 3-20, 2005.

Carrasco-Núñez, G., Gómez-Tuena, A., and Lozano, L.: Geologic map of Cerro Grande volcano and surrounding area, Central México. Geological Society of America Maps and Charts series MCH 081, pp. 10, 1997.

Carrasco-Núñez, G., Siebert, L., Díaz-Castellón, R., Vázquez-Selem, L., Capra, L.: Evolution and hazards of a long-quiescent compound shield-like volcano: Cofre de Perote, Eastern Trans-Mexican Volcanic Belt. J. Volcanol. Geoth. Res., 197, 209-224, http://dx.doi.org/10.1016/j.jvolgeores.2009.08.010, 2010.

Carrasco-Núñez, G., Dávila-Harris, P., Riggs, N. R., Ort, M. H., Zimmer, B. W., Willcox, C. P., and Branney, M. J.: Recent explosive volcanism at the Eastern Trans-Mexican Volcanic Belt, in: Aranda-Gómez, J. J., Tolson, G., and Molina-Garza, R. S. (eds.), The Southern Cordillera and Beyond. Geological Society of America Field Guide 25, p. 83–113, doi:10.1130/2012.0025(05), 2012a.

Carrasco-Núñez, G., McCurry, M., Branney, M. J., Norry, M., and Willcox, C.: Complex magma mixing, mingling, and withdrawal associated with an intra-Plinian ignimbrite eruption at a large silicic caldera volcano: Los Humeros of central Mexico. Geol. Soc. Am. Bull., 124(11-12), 1793-1809, 2012b.

Carrasco-Núñez, G., López-Martínez, M., Hernández, J., and Vargas, V.: Subsurface stratigraphy and its correlation with the surficial geology at Los Humeros geothermal field, eastern Trans-Mexican Volcanic Belt. Geothermics, 67, 1-17, 2017a.

Carrasco-Núñez, G., Hernández, J., De León, L., Dávila, P., Norini, G., Bernal, J. P., Jicha, B., Navarro, M., and López-Quiroz, P.: Geologic Map of Los Humeros volcanic complex and geothermal field, eastern Trans-Mexican Volcanic Belt/Mapa geológico del complejo volcánico Los Humeros y campo geotérmico, sector oriental del Cinturón Volcánico Trans-Mexicano. Terradigitalis, 1, 1-11. DOI: 10.22201/igg.terradigitalis.2017.2.24.78, 2017b.

Carrasco-Núñez, G., Bernal, J. P., Davila, P., Jicha, B., Giordano, G., and Hernández, J.: Reappraisal of Los Humeros volcanic complex by new U/Th zircon and $^{40}Ar/^{39}Ar$ dating: Implications for greater geothermal potential. Geochem. Geophy. Geosy., 19, 132-149, 2018.

Cashman, K. V.: Groundmass crystallization of Mount St. Helens dacite, 1980–1986: a tool for interpreting shallow magmatic processes. Contrib. Mineral. Petr., 109, 431-449, 1992.

Cashman, K., and Blundy, J.: Degassing and crystallization of ascending andesite and dacite. Philos. T. Roy. Soc. A, 358, 1487-1513, 2000.

Cashman, K. V., and Giordano, G.: Calderas and magma reservoirs. J. Volcanol. Geoth. Res., 288, 28-45, 2014.

Cashman, K. V., Sparks, R. S. J., and Blundy, J. D.: Vertically extensive and unstable magmatic systems: a unified view of igneous processes. Science, 355, eaag3055, 2017.

Chadwick, J. P., Troll, V. R., Waight, T. E., van der Zwan, F. M., and Schwarzkopf, L. M.: Petrology and geochemistry of igneous inclusions in recent Merapi deposits: a window into the sub-volcanic plumbing system. Contrib. Mineral. Petr., 165, 259-282, 2013.

Charlier, B. L. A., Bachmann, O., Davidson, J. P., Dungan, M. A., and Morgan, D. J.: The upper crustal evolution of a large silicic magma body: evidence from crystal-scale Rb–Sr isotopic heterogeneities in the Fish Canyon magmatic system, Colorado. J. Petrol., 48, 1875-1894, 2007.

Clague, D. A., Moore, J. G., Dixon, J. E., and Friesen, W. B.: Petrology of submarine lavas from Kilauea's Puna Ridge, Hawaii. Oceanogr. Lit. Rev., 10, 857-858, 1995.

Clarke, A. B., Stephens, S., Teasdale, R., Sparks, R. S. J., and Diller, K.: Petrologic constraints on the decompression history of magma prior to Vulcanian explosions at the Soufrière Hills volcano, Montserrat. J. Volcanol. Geoth. Res., 161, 261-274, 2007.

Coombs, M. L., and Gardner, J. E.: Shallow-storage conditions for the rhyolite of the 1912 eruption at Novarupta, Alaska. Geology, 29, 775-778, 2001.

Coombs, M. L., and Gardner, J. E.: Reaction rim growth on olivine in silicic melts: Implications for magma mixing. Am. Mineral., 89, 748-758, 2004.

Costa, F., Andreastuti, S., de Maisonneuve, C. B., and Pallister, J. S.: Petrological insights into the storage conditions, and magmatic processes that yielded the centennial 2010 Merapi explosive eruption. J. Volcanol. Geoth. Res., 261, 209-235, 2013.

Crawford, A. J., Falloon, T. J., and Eggins, S.: The origin of island arc high-alumina basalts. Contrib. Mineral. Petr., 97, 417-430, 1987.

Créon, L., Levresse, G., Carrasco-Nuñez, G., and Remusat, L.: Evidence of a shallow magma reservoir below Los Humeros volcanic complex: Insights from the geochemistry of silicate melt inclusions. J. S. Am. Earth Sci., 88, 446-458, 2018.

Dahren, B., Troll, V. R., Andersson, U. B., Chadwick, J. P., Gardner, M. F., Jaxybulatov, K., and Koulakov, I.: Magma plumbing beneath Anak Krakatau volcano, Indonesia: evidence for multiple magma storage regions. Contrib. Mineral. Petr., 163, 631-651, 2012.

Daubeny, C. G. B.: Some account of the eruption of Vesuvius, which occurred in the month of August, 1834, extracted from the manuscript notes of the cavaliere monticelli, foreign associate of the Geological Society, and from other sources; together with a statement of the products of the eruption, and of the condition of the volcano subsequently to it. In: Abstracts of the Papers Printed in the Philosophical Transactions of the Royal Society of London, London: The Royal Society, 3, 326-327, 1837.

Davies, J. H.: Global map of solid Earth surface heat flow. Geochem. Geophy. Geosy., 14, 4608-4622, 2013.

Dávila-Harris, P., and Carrasco-Núñez, G.: An unusual syn-eruptive bimodal eruption: the Holocene Cuicuiltic Member at Los Humeros caldera, Mexico. J. Volcanol. Geoth. Res., 271, 24-42, 2014.

Demant, A.: Características del Eje Neovolcánico Transmexicano y sus problemas de interpretación. Rev. Mex. Cienc. Geol., 2, 172-187, 1978.

Di Renzo, V., Wohletz, K., Civetta, L., Moretti, R., Orsi, G., and Gasparini, P.: The thermal regime of the Campi Flegrei magmatic system reconstructed through 3D numerical simulations. J. Volcanol. Geoth. Res., 328, 210-221, 2016.

Donaldson, C. H.: Olivine crystal types in harrisitic rocks of the Rhum pluton and in Archean spinifex rocks. Geol. Soc. Am. Bull., 85, 1721-1726, 1974.

Duda, A., and Schmincke, H. U.: Polybaric differentiation of alkali basaltic magmas: evidence from green-core clinopyroxenes (Eifel, FRG). Contrib. Mineral. Petr., 91, 340-353, 1985.

Duffield, W. A., and Sass, J. H.: Geothermal energy: Clean power from the earth's heat (Vol. 1249, p. 34). Reston, VA: U.S. Geothermal Development, US Geological Survey, 2003.

Dungan, M. A., Long, P. E., and Rhodes, J. M.: Magma mixing at mid-ocean ridges: Evidence from legs 45 and 46-DSDP. Geophys. Res. Lett., 5, 423-425, 1978.

Dziewonski, A. M., and Anderson, D. L.: Preliminary reference Earth model. Phys. Earth Planet. In., 25, 297-356, 1981.

Elardo, S. M., and Shearer, C. K.: Magma chamber dynamics recorded by oscillatory zoning in pyroxene and olivine phenocrysts in basaltic lunar meteorite Northwest Africa 032. Am. Mineral., 99, 355-368, 2014.

Ellis, B. S., Szymanowski, D., Wotzlaw, J. F., Schmitt, A. K., Bindeman, I. N., Troch, J., Harris, C., Bachmann, O., and Guillong, M..: Post-caldera volcanism at the Heise volcanic field: implications for petrogenetic models. J. Petrol., 58, 115-136, 2017.

Eskandari, A., Amini, S., De Rosa, R., and Donato, P.: Nature of the magma storage system beneath the Damavand volcano (N. Iran): An integrated study. Lithos, 300, 154-176, 2018.

Falloon, T. J., and Green, D. H.: Anhydrous partial melting of MORB pyrolite and other peridotite compositions at 10 kbar: implications for the origin of primitive MORB glasses. Miner. Petrol., 37(3-4), 181-219, 1987.

Faure, F., Trolliard, G., Nicollet, C., and Montel, J. M.: A developmental model of olivine morphology as a function of the cooling rate and the degree of undercooling. Contrib. Mineral. Petr., 145(2), 251-263, 2003.

Feng, W., and Zhu, Y.: Decoding magma storage and pre-eruptive processes in the plumbing system beneath early Carboniferous arc volcanoes of southwestern Tianshan, Northwest China. Lithos, 322, 362-375, 2018.

Ferrari, L., López-Martínez, M., Aguirre-Díaz, G., and Carrasco-Núñez, G.: Space-time patterns of Cenozoic arc volcanism in Central Mexico: from the Sierra Madre Occidental to the Mexican Volcanic Belt. Geology, 27, 303-306, 1999.

Ferrari, L., Orozco-Esquivel, T., Manea, V., Manea, M.: The dynamic history of the Trans-Mexican Volcanic Belt and the Mexico subduction zone. Tectonophysics, 522, 122-149, 2012.

Ferriz, H., and Mahood, G. A.: Eruption rates and compositional trends at Los Humeros volcanic center, Puebla, Mexico. J. Geophys. Res-Sol. Ea., 89(B10), 8511-8524, 1984.

Ferriz, H., and Mahood, G. A.: Strong compositional zonation in a silicic magmatic system: Los Humeros, Mexican Neovolcanic Belt. J. Petrol., 28, 171-209, 1987.

Fitz-Díaz, E., Lawton, T. F., Juárez-Arriaga, E., and Chávez-Cabello, G.: The Cretaceous-Paleogene Mexican orogen: Structure, basin development, magmatism and tectonics. Earth-Sci. Rev., 183, 56-84, 2018.

Fowler, A. D., Berger, B., Shore, M., Jones, M. I., and Ropchan, J.: Supercooled rocks: development and significance of varioles, spherulites, dendrites and spinifex in Archaean volcanic rocks, Abitibi Greenstone belt, Canada. Precambrian Res., 115, 311-328, 2002.

Freundt, A., and Schmincke, H. U.: Petrogenesis of rhyolite-trachyte-basalt composite ignimbrite P1, Gran Canada, Canary Islands. J. Geophys. Res-Sol. Ea., 100(B1), 455-474, 1995.

Fujii, T., and Scarfe, C. M.: Composition of liquids coexisting with spinel lherzolite at 10 kbar and the genesis of MORBs. Contrib. Mineral. Petr., 90, 18-28, 1985.

Galipp, K., Klügel, A., and Hansteen, T. H.: Changing depths of magma fractionation and stagnation during the evolution of an oceanic island volcano: La Palma (Canary Islands). J. Volcanol. Geoth. Res., 155, 285-306, 2006.

Gao, J. F., and Zhou, M. F.: Generation and evolution of siliceous high magnesium basaltic magmas in the formation of the Permian Huangshandong intrusion (Xinjiang, NW China). Lithos, 162, 128-139, 2013.

Gardner, M. F., Troll, V. R., Gamble, J. A., Gertisser, R., Hart, G. L., Ellam, R. M., Harris, C., and Wolf, J. A.: Shallow level differentiation processes at Krakatau: evidence for late-stage crustal contamination. J. Petrol., 54, 149-182, 2013.

Gernon, T. M., Upton, B. G. J., Ugra, R., Yücel, C., Taylor, R. N., and Elliott, H.: Complex subvolcanic magma plumbing system of an alkali basaltic maar-diatreme volcano (Elie Ness, Fife, Scotland). Lithos, 264, 70-85, 2016.

Ginibre, C., Wörner, G., and Kronz, A.: Crystal zoning as an archive for magma evolution. Elements, 3, 261-266, 2007.

Giordano, G., Lucci, F., Phillips, D., Cozzupoli, D., and Runci, V.: Stratigraphy, geochronology and evolution of the Mt. Melbourne volcanic field (North Victoria Land, Antarctica). B. Volcanol., 74, 1985-2005, 2012.

Giuffrida, M., and Viccaro, M.: Three years (2011–2013) of eruptive activity at Mt. Etna: working modes and timescales of the modern volcano plumbing system from micro-analytical studies of crystals. Earth-Sci. Rev., 171, 289-322, 2017.

Glazner, A. F., Bartley, J. M., Coleman, D. S., Gray, W., and Taylor, R. Z.: Are plutons assembled over millions of years by amalgamation from small magma chambers? GSA today, 14, 4-12, 2004.

Gómez-Tuena, A., and Carrasco-Núñez, G.: Cerro Grande volcano: the evolution of a Miocene stratocone in the early Trans-Mexican Volcanic Belt, Tectonophysics, 318, 249-280, 2000.

Gómez-Tuena, A., LaGatta, A.B., Langmuir, C.H., Goldstein, S.L., Ortega-Gutiérrez, F., Carrasco-Núñez, G.: Temporal control of subduction magmatism in the eastern Trans-Mexican Volcanic Belt: mantle sources, slab contributions, and crustal contamination. Geochem. Geophy. Geosy., 4. http://dx.doi.org/10. 1029/2003GC000524, 2003.

Gómez-Tuena, A., Langmuir, C.H., Goldstein, S.L., Straub, S., Ortega-Gutiérrez, F.: Geochemical evidence for slab melting in the Trans-Mexican Volcanic Belt. J. Petrol., 48, 537–562, 2007a.

Gómez-Tuena, A., Orozco-Esquivel, M.T., Ferrari, L.: Igneous petrogenesis of the Transmexican Volcanic Belt. In: Alaniz-Álvarez, S.A., Nieto-Samaniego, A.F. (Eds.), Geology of México: Celebrating the Centenary of the Geological Society of México. Geol. S. Am. S., 422, 129–181, 2007b.

Gómez-Tuena, A., Mori, L., Straub, S.: Geochemical and petrological insights into the tectonic origin of the Transmexican Volcanic Belt, Earth-Sci. Rev. 183, 153-181. http://dx.doi.org/10.1016/j.earscirev.2016.12.006, 2018.

Gregg, P. M., De Silva, S. L., Grosfils, E. B., and Parmigiani, J. P.: Catastrophic caldera-forming eruptions: Thermomechanics and implications for eruption triggering and maximum caldera dimensions on Earth. J. Volcanol. Geoth. Res., 241, 1-12, 2012.

Grove, T. L.: Origin of Magmas, Encyclopedia of Volcanoes, 133-148, 2000.

Grove, T. L., Gerlach, D. C., and Sando, T. W.: Origin of calc-alkaline series lavas at Medicine Lake volcano by fractionation, assimilation and mixing. Contrib. Mineral. Petr., 80, 160-182, 1982.

Grove, T. L., Donnelly-Nolan, J. M., and Housh, T.: Magmatic processes that generated the rhyolite of Glass Mountain, Medicine Lake volcano, N. California. Contrib. Mineral. Petr., 127, 205-223, 1997.

Gualda, G. A., and Ghiorso, M. S.: The Bishop Tuff giant magma body: an alternative to the Standard Model. Contrib. Mineral. Petr., 166, 755-775, 2013.

Gunnarsson, G., and Aradóttir, E. S.: The deep roots of geothermal systems in volcanic areas: boundary conditions and heat sources in reservoir modeling. Transport in Porous Media, 108, 43-59, 2015.

Herzberg, C., and O'Hara, M. J.: Plume-associated ultramafic magmas of Phanerozoic age. J. Petrol., 43, 1857-1883, 2002.

Hildreth, W.: The Bishop Tuff: Evidence for the origin of compositional zonation in silicic magma chambers. Geol. S. Am. S., 180, 43-75, 1979.

Hildreth, W.: Gradients in silicic magma chambers: implications for lithospheric magmatism. J. Geophys. Res-Sol. Ea., 86(B11), 10153-10192, 1981.

Hildreth, W., and Wilson, C. J.: Compositional zoning of the Bishop Tuff. J. Petrol., 48, 951-999, 2007.

Holland, T., and Powell, R.: Plagioclase feldspars: activity-composition relations based upon Darken's quadratic formalism and Landau theory. Am. Mineral., 77, 53-61, 1992.

Holland, T., and Blundy, J.: Non-ideal interactions in calcic amphiboles and their bearing on amphibole-plagioclase thermometry. Contrib. Mineral. Petr., 116, 433-447, 1994.

Humphreys, M. C., Blundy, J. D., and Sparks, R. S. J.: Magma evolution and open-system processes at Shiveluch Volcano: Insights from phenocryst zoning. J. Petrol., 47, 2303-2334, 2006.

Humphreys, M. C., Christopher, T., and Hards, V.: Microlite transfer by disaggregation of mafic inclusions following magma mixing at Soufrière Hills volcano, Montserrat. Contrib. Mineral. Petr., 157, 609-624, 2009.

Huraiová, M., Konečný, P., Holický, I., Milovská, S., Nemec, O., and Hurai, V.: Mineralogy and origin of peralkaline granite-syenite nodules ejected in Pleistocene basalt from Bulhary, southern Slovakia. Period. Mineral., 86, 1-17, 2017.

Jeffery, A. J., Gertisser, R., Troll, V. R., Jolis, E. M., Dahren, B., Harris, C., Tindle, A. G., Preece, K., O'Driscoll, B., Humaida, H., and Chadwick, J. P.: The pre-eruptive magma plumbing system of the 2007–2008 dome-forming eruption of Kelut volcano, East Java, Indonesia. Contrib. Mineral. Petr., 166, 275-308, 2013.

Jellinek, A. M., and DePaolo, D. J.: A model for the origin of large silicic magma chambers: precursors of caldera-forming eruptions. B. Volcanol., 65, 363-381, 2003.

Keiding, J. K., and Sigmarsson, O.: Geothermobarometry of the 2010 Eyjafjallajökull eruption: New constraints on Icelandic magma plumbing systems. J. Geophys. Res-Sol. Ea., 117(B9), doi:10.1029/2011JB008829, 2012.

Kelley, D. F., and Barton, M.: Pressures of crystallization of Icelandic magmas. J. Petrol., 49, 465-492, 2008.

Kinzler, R. J., Donnelly-Nolan, J. M., and Grove, T. L.: Late Holocene hydrous mafic magmatism at the Paint Pot Crater and Callahan flows, Medicine Lake Volcano, N. California and the influence of H 2 O in the generation of silicic magmas. Contrib. Mineral. Petr., 138, 1-16, 2000.

Klügel, A., Hoernle, K. A., Schmincke, H. U., and White, J. D.: The chemically zoned 1949 eruption on La Palma (Canary Islands): Petrologic evolution and magma supply dynamics of a rift zone eruption. J. Geophys. Res-Sol. Ea., 105(B3), 5997-6016, 2000.

Klügel, A., Hansteen, T. H., and Galipp, K.: Magma storage and underplating beneath Cumbre Vieja volcano, la Palma (Canary Islands). Earth Planet. Sc. Lett., 236, 211-226, 2005.

Kratzmann, D. J., Carey, S., Scasso, R., and Naranjo, J. A.: Compositional variations and magma mixing in the 1991 eruptions of Hudson volcano, Chile. B. Volcanol., 71, 419-439, DOI:10.1007/s00445-008-0234-x, 2009.

Kushiro, I.: The system forsterite-diopside-silica with and without water at high pressures. Am. J. Sci., 267(A), 269-294, 1969.

Kushiro, I., and Yoder, H. S., Jr.: Melting of forsterite and enstatite at high pressures and hydrous conditions. Carnegie Inst. Wash. Yrbk., 67, 153-158, 1969.

Lange, R. A., Frey, H. M., and Hector, J.: A thermodynamic model for the plagioclase-liquid hygrometer/thermometer. Am. Mineral., 94, 494-506, 2009.

Langmuir, C. H., and Hanson, G. N.: An evaluation of major element heterogeneity in the mantle sources of basalts. Philos. Tr. R. Soc. S-A, 297(1431), 383-407, 1980.

Laumonier, M., Scaillet, B., Arbaret, L., and Champallier, R.: Experimental simulation of magma mixing at high pressure. Lithos, 196, 281-300, 2014.

Le Maitre, R. W., Streckeisen, A., Zanettin, B., Le Bas, M. J., Bonin, B., Bateman, P., Bellieni, G., Dudek, A., Efremova, S., Keller, J., Lameyre, J., Sabine, P. A., Schmid, R., Sqrensen, H., Woolley, A. R.: Igneous Rocks. A Classification and Glossary of terms. Recommendations of the IUGS Subcommission on the Systematics of Igneous Rocks, CambridgeUniversity Press, pp. 236, 2002.

Lindsley, D. H.: Pyroxene thermometry. Am. Mineral., 68, 477-493, 1983.

Lucci, F., Rossetti, F., Becchio, R., Theye, T., Gerdes, A., Opitz, J., Baez, W., Bardelli, L., De Astis, G., Viramonte, J., and Giordano, G.: Magmatic Mn-rich garnets in volcanic settings: Age and longevity of the magmatic plumbing system of the Miocene Ramadas volcanism (NW Argentina). Lithos, 322, 238-249, 2018.

Macdonald, R., Bagiński, B., Ronga, F., Dzierżanowski, P., Lustrino, M., Marzoli, A., and Melluso, L.: Evidence for extreme fractionation of peralkaline silicic magmas, the Boseti volcanic complex, Main Ethiopian Rift. Miner. Petrol., 104, 163-175, 2012.

Maclennan, J., McKenzie, D., Gronvöld, K., and Slater, L.: Crustal accretion under northern Iceland. Earth Planet. Sc. Lett., 191, 295-310, 2001.

Martinez, M., Fernindez, R., Visquez, R., Vega, R., Reyes, S. A.: Asimilacion del metodo magnetotelurico para la exploracion geotermica. Quinto informe tecnico CICESE-IIE, Mexico, 1983.

Masotta, M., Mollo, S., Freda, C., Gaeta, M., and Moore, G.: Clinopyroxene–liquid thermometers and barometers specific to alkaline differentiated magmas. Contrib. Mineral. Petr., 166, 1545-1561, 2013.

Matthews, N. E., Vazquez, J. A., Calvert, A. T.: Age of the Lava Creek supereruption and magma chamber assembly at Yellowstone based on $^{40}Ar/^{39}Ar$ and U-Pb dating of sanidine and zircon crystals. Geochem. Geophy. Geosy., 16, 2508–2528, 2015.

Melluso, L., Morra, V., Guarino, V., De'Gennaro, R., Franciosi, L., and Grifa, C.: The crystallization of shoshonitic to peralkaline trachyphonolitic magmas in a H_2O–Cl–F-rich environment at Ischia (Italy), with implications for the feeder system of the Campania Plain volcanoes. Lithos, 210, 242-259, 2014.

Mollo, S., Del Gaudio, P., Ventura, G., Iezzi, G., and Scarlato, P.: Dependence of clinopyroxene composition on cooling rate in basaltic magmas: implications for thermobarometry. Lithos, 118, 302-312, 2010.

Mordick, B. E., and Glazner, A. F.: Clinopyroxene thermobarometry of basalts from the Coso and Big Pine volcanic fields, California. Contrib. Mineral. Petr., 152, 111-124, 2006.

Morimoto, N.: Nomenclature of pyroxenes. Am. Mineral., 73, 1123-1133, 1988.

Morimoto, N.: Nomenclature of pyroxenes. Mineral. J., 14, 198-221, 1989.

Mutch, E. J. F., Blundy, J. D., Tattitch, B. C., Cooper, F. J., and Brooker, R. A.: An experimental study of amphibole stability in low-pressure granitic magmas and a revised Al-in-hornblende geobarometer. Contrib. Mineral. Petr., 171:85, 1-27, https://doi.org/10.1007/s00410-016-1298-9, 2016.

Nairn, I. A., Kobayashi, T., and Nakagawa, M.: The ~10 ka multiple vent pyroclastic eruption sequence at Tongariro Volcanic Centre, Taupo Volcanic Zone, New Zealand: Part 1. Eruptive processes during regional extension. J. Volcanol. Geoth. Res., 86, 19-44, 1998.

Nakagawa, M., Nairn, I. A., and Kobayashi, T.: The similar to 10 ka multiple vent pyroclastic eruption sequence at Tongariro Volcanic Centre, Taupo Volcanic Zone, New Zealand: Part 2. Petrological insights into magma storage and transport during regional extension. J. Volcanol. Geoth. Res., 86, 45-65, 1998.

Namur, O., Charlier, B., Toplis, M. J., and Vander Auwera, J.: Prediction of plagioclase-melt equilibria in anhydrous silicate melts at 1-atm. Contrib. Mineral. Petr., 163, 133-150, 2012.

Neave, D. A., Maclennan, J., Hartley, M. E., Edmonds, M., and Thordarson, T.: Crystal storage and transfer in basaltic systems: the Skuggafjöll eruption, Iceland. J. Petrol., 55, 2311-2346, 2014.

Negendak, J. F. W., Emmermann, R., Krawczyk, R., Mooser, F., Tobschall, H., and Werle, D.: Geological and geochemical investigations on the eastern trans mexican volcanic belt. Geofis. Int., 24, 477-575, 1985.

Nimis, P.: A clinopyroxene geobarometer for basaltic systems based on crystal-structure modeling. Contrib. Mineral. Petr., 121, 115-125, 1995.

Norini, G., Groppelli, G., Sulpizio, R., Carrasco-Núñez, G., Dávila-Harris, P., Pellicioli, C., Zucca, F., and De Franco, R.: Structural analysis and thermal remote sensing of the Los Humeros Volcanic Complex: Implications for volcano structure and geothermal exploration. J. Volcanol. Geoth. Res., 301, 221-237, 2015.

Pamukcu, A. S., Gualda, G. A., Bégué, F., and Gravley, D. M.: Melt inclusion shapes: Timekeepers of short-lived giant magma bodies. Geology, 43, 947-950, 2015.

Patanè, D., De Gori, P., Chiarabba, C., and Bonaccorso, A.: Magma ascent and the pressurization of Mount Etna's volcanic system. Science, 299, 2061-2063, 2003.

Petrone, C. M., Bugatti, G., Braschi, E., and Tommasini, S.: Pre-eruptive magmatic processes re-timed using a non-isothermal approach to magma chamber dynamics. Nat. Commun., 7, 12946, 2016.

Pietruszka, A. J., and Garcia, M. O.: The size and shape of Kilauea Volcano's summit magma storage reservoir: a geochemical probe. Earth Planet. Sc. Lett., 167, 311-320, 1999.

Preece, K., Barclay, J., Gertisser, R., and Herd, R. A.: Textural and micro-petrological variations in the eruptive products of the 2006 dome-forming eruption of Merapi volcano, Indonesia: implications for sub-surface processes. J. Volcanol. Geoth. Res., 261, 98-120, 2013.

Presnall, D. C., Dixon, S. A., Dixon, J. R., O'Donnell, T. H., Brenner, N. L., Schrock, R. L., and Dycus, D. W.: Liquidus phase relations on the join diopside-forsterite-anorthite from 1 atm to 20 kbar: their bearing on the generation and crystallization of basaltic magma. Contrib. Mineral. Petr., 66, 203-220, 1978.

Putirka, K.: Magma transport at Hawaii: Inferences based on igneous thermobarometry. Geology, 25, 69-72, 1997.

Putirka, K.: Clinopyroxene+liquid equilibria to 100 kbar and 2450 K. Contrib. Mineral. Petr., 135, 151-163, 1999.

Putirka, K. D.: Mantle potential temperatures at Hawaii, Iceland, and the mid-ocean ridge system, as inferred from olivine phenocrysts: Evidence for thermally driven mantle plumes. Geochem. Geophy. Geosy., 6, doi:10.1029/2005GC000915, 2005a.

Putirka, K. D.: Igneous thermometers and barometers based on plagioclase+ liquid equilibria: Tests of some existing models and new calibrations. Am. Mineral., 90, 336-346, 2005b.

Putirka, K. D.: Thermometers and barometers for volcanic systems. Rev. Mineral. Geochem., 69, 61-120, 2008.

Putirka, K., Johnson, M., Kinzler, R., Longhi, J., and Walker, D.: Thermobarometry of mafic igneous rocks based on clinopyroxene-liquid equilibria, 0–30 kbar. Contrib. Mineral. Petr., 123, 92-108, 1996.

Putirka, K., Ryerson, F. J., and Mikaelian, H.: New igneous thermobarometers for mafic and evolved lava compositions, based on clinopyroxene+ liquid equilibria. Am. Mineral., 88, 1542-1554, 2003.

Putirka, K. D., Perfit, M., Ryerson, F. J., and Jackson, M. G.: Ambient and excess mantle temperatures, olivine thermometry, and active vs. passive upwelling. Chem. Geol., 241, 177-206, 2007.

Redman, B. A., and Keays, R. R.: Archaean basic volcanism in the eastern Goldfields province, Yilgarn Block, western Australia. Precambrian Res., 30, 113-152, 1985.

Reubi, O., and Nicholls, I. A.: Magmatic evolution at Batur volcanic field, Bali, Indonesia: petrological evidence for polybaric fractional crystallization and implications for caldera-forming eruptions. J. Volcanol. Geoth. Res., 138, 345-369, 2004.

Rhodes, J. M., Dungan, M. A., Blanchard, D. P., and Long, P. E.: Magma mixing at mid-ocean ridges: evidence from basalts drilled near 22 N on the Mid-Atlantic Ridge. Tectonophysics, 55, 35-61, 1979.

Rivera, T. A., Schmitz, M. D., Crowley, J. L., and Storey, M.: Rapid magma evolution constrained by zircon petrochronology and $^{40}Ar/^{39}Ar$ sanidine ages for the Huckleberry Ridge Tuff, Yellowstone, USA, Geology, 42, 643-646, 2014.

Roeder, P. L., and Emslie, R.: Olivine-liquid equilibrium. Contrib. Mineral. Petr., 29, 275-289, 1970.

Rojas-Ortega, E.: Litoestratigrafìa, petrografìa y geoquìmica de la toba Llano, y su relacìon con el crater el Xalapazco, Caldera de LosHumeros, Puebla. MS Thesis, IPICYT, San Luis Potosí, México, pp. 129, 2016.

Romo-Jones, J. M., Gutiérrez-Negrín, L. C. A., Flores-Armenta, M., Del Valle, J. L., and García, A: Mexico, in: 2017 Annual Report, IEA Geothermal, 66–72, available at: https://drive.google.com/file/d/1ztLlE5MFdLwSndR7iLmAkMXnQth4c86T/view, 2017.

Ronga, F., Lustrino, M., Marzoli, A., and Melluso, L.: Petrogenesis of a basalt-comendite-pantellerite rock suite: the Boseti Volcanic Complex (Main Ethiopian Rift). Miner. Petrol., 98, 227-243, 2010.

Rutherford, M. J., Sigurdsson, H., Carey, S., and Davis, A.: The May 18, 1980, eruption of Mount St. Helens: 1. Melt composition and experimental phase equilibria. J. Geophys. Res-Sol. Ea., 90(B4), 2929-2947, 1985.

Schmidt, M. W.: Amphibole composition in tonalite as a function of pressure: an experimental calibration of the Al-in-hornblende barometer. Contrib. Mineral. Petr., 110, 304-310, 1992.

Scott, J. A., Mather, T. A., Pyle, D. M., Rose, W. I., and Chigna, G.: The magmatic plumbing system beneath Santiaguito Volcano, Guatemala. J. Volcanol. Geoth. Res., 237, 54-68, 2012.

Shane, P., and Coote, A.: Thermobarometry of Whangarei volcanic field lavas, New Zealand: Constraints on plumbing systems of small monogenetic basalt volcanoes. J. Volcanol. Geoth. Res., 354, 130-139, 2018.

Sigmarsson, O., Vlastélic, I., Andreasen, R., Bindeman, I., Devidal, J. L., Moune, S., Keiding, J. K., Larsen, G., Hoskuldsson, A., and Thordarson, T.: Dynamic magma mixing revealed by the 2010 Eyjafjallajökull eruption. Solid Earth Discussions, 3, 591-613, 2011.

Sisson, T. W., and Grove, T. L.: Temperatures and H_2O contents of low-MgO high-alumina basalts. Contrib. Mineral. Petr., 113, 167-184, 1993.

Sisson, T. W., and Layne, G. D.: H_2O in basalt and basaltic andesite glass inclusions from four subduction-related volcanoes. Earth Planet. Sc. Lett., 117, 619-635, 1993.

Smith, R. L., and Shaw, H. R.: Igneous-related geothermal systems. US Geological Survey Circular 726, 58-83, 1975.

Stroncik, N. A., Klügel, A., and Hansteen, T. H.: The magmatic plumbing system beneath El Hierro (Canary Islands): constraints from phenocrysts and naturally quenched basaltic glasses in submarine rocks. Contrib. Mineral. Petr., 157, 593-607, DOI:10.1007/s00410-008-0354-5, 2009.

Suter, M.: Structural traverse across the Sierra Madre Oriental fold-thrust belt in east-central Mexico. Geol. Soc. Am. Bull., 98(3), 249-264, 1987.

Takahashi, E.: Melting of a dry peridotite KLB-1 up to 14 GPa: Implications on the origin of peridotitic upper mantle. J. Geophys. Res-Sol. Ea., 91(B9), 9367-9382, 1986.

Thompson, R. N.: Primary basalts and magma genesis. Contrib. Mineral. Petr., 45, 317-341, 1974.

Thornber, C. R., Heliker, C., Sherrod, D. R., Kauahikaua, J. P., Miklius, A., Okubo, P. G., Trusdell, F. A., Budhan, J. R., Ridley, W. I. and Meeker, G. P.: Kilauea east rift zone magmatism: An episode 54 perspective. J. Petrol., 44, 1525-1559, 2003.

Troll, V. R., Deegan, F. M., Jolis, E. M., Harris, C., Chadwick, J. P., Gertisser, R., Schwarzkopf, L. M., Borisova, A., Bindeman, I. N., Sumarti, S., and Preece, K.: Magmatic differentiation processes at Merapi Volcano: inclusion petrology and oxygen isotopes. J. Volcanol. Geoth. Res., 261, 38-49, 2013.

Ubide, T., Gale, C., Arranz, E., Lago, M., and Larrea, P.: Clinopyroxene and amphibole crystal populations in a lamprophyre sill from the Catalonian Coastal Ranges (NE Spain): a record of magma history and a window to mineral-melt partitioning. Lithos, 184, 225-242, 2014.

Verma, S. P.: Magma genesis and chamber processes at Los Humeros caldera, Mexico—Nd and Sr isotope data. Nature, 302(5903), 52, 1983.

Verma, S. P.: Alkali and alkaline earth element geochemistry of Los Humeros caldera, Puebla, Mexico. J. Volcanol. Geoth. Res., 20, 21–40, 1984.

Verma, S. P.: Heat source in Los Humeros geothermal area, Puebla, Mexico. Geoth. Res. T., 9, 521-525, 1985a.

Verma, S. P.: On the magma chamber characteristics as inferred from surface geology and geochemistry: examples from Mexican geothermal areas. Phys. Earth Planet. In., 41, 207-214, 1985b.

Verma, S. P.: Geochemical evidence for a lithospheric source for magmas from Los Humeros caldera, Puebla, Mexico. Chem. Geol., 164, 35-60, 2000.

Verma, S. P., and López, M.: Geochemistry of Los Humeros caldera, Puebla, Mexico. B. Volcanol., 45, 63-79, 1982.

Verma M. P., Verma, S. P. and Sanvincente, H.: Temperature field simulation with stratification model of magma chamber under Los Humeros caldera, Puebla, Mexico. Geothermics, 19, 187-197, 1990.

Verma, S. P., and Andaverde, J.: Temperature field distribution from cooling of a magma chamber. Proceeding World Geothermal Congress, 1119-1121, 1995.

Verma, S. P., Gomez-Arias, E. and Andaverde J.: Thermal sensitivity analysis of emplacement of the magma chamber in Los Humeros caldera, Puebla, Mexico. Int. Geol. Rev., 53, 905-925, 2011.

Verma, S. P. and Gomez-Arias, E.: Three-dimensional temperature field simulation of magma chamber in the Los Humeros geothermal field, Puebla, Mexico. Appl. Therm. Eng., 52, 512-515, 2013.

Viccaro, M., Calcagno, R., Garozzo, I., Giuffrida, M., and Nicotra, E.: Continuous magma recharge at Mt. Etna during the 2011–2013 period controls the style of volcanic activity and compositions of erupted lavas. Miner. Petrol., 109, 67-83, 2015.

Viccaro, M., Barca, D., Bohrson, W. A., D'Oriano, C., Giuffrida, M., Nicotra, E., and Pitcher, B. W.: Crystal residence times from trace element zoning in plagioclase reveal changes in magma transfer dynamics at Mt. Etna during the last 400 years. Lithos, 248, 309-323, 2016.

Vidal, O., Parra, T., and Vieillard, P.: Thermodynamic properties of the Tschermak solid solution in Fe-chlorite: Application to natural examples and possible role of oxidation. Am. Mineral., 90, 347-358, 2005.

Viniegra-Osorio, F.: Geología del Macizo de Teziutlán y la Cuenca Cenozoica de Veracruz. Asoc. Mex. Geológos Petroleros Bol., 17, 101-163, 1965.

Wagner, T. P., Donnelly-Nolan, J. M., and Grove, T. L.: Evidence of hydrous differentiation and crystal accumulation in the low-MgO, high-Al_2O_3 lake basalt from Medicine Lake volcano, California. Contrib. Mineral. Petr., 121, 201-216, 1995.

Wallace, P., and Anderson, A. T. Jr.: Volatiles in Magmas. Encyclopedia of Volcanoes, 149–170, 2000.

Waters, L. E., and Lange, R. A.: An updated calibration of the plagioclase-liquid hygrometer-thermometer applicable to basalts through rhyolites. Am. Mineral., 100, 2172-2184, 2015.

Welsch, B., Faure, F., Famin, V., Baronnet, A., and Bachèlery, P.: Dendritic crystallization: A single process for all the textures of olivine in basalts? J. Petrol., 54, 539-574, 2013.

White, J. C., Ren, M., and Parker, D. F.: Variation in mineralogy, temperature, and oxygen fugacity in a suite of strongly peralkaline lavas and tuffs, Pantelleria, Italy. Can. Mineral., 43, 1331-1347, 2005.

White, J. C., Parker, D. F., and Ren, M.: The origin of trachyte and pantellerite from Pantelleria, Italy: insights from major element, trace element, and thermodynamic modelling. J. Volcanol. Geoth. Res., 179, 33-55, 2009.

Whitney, D. L., and Evans, B. W.: Abbreviations for names of rock-forming minerals. Am. Mineral., 95(1), 185-187, 2010.

Wilcox, C.: Eruptive, Magmatic and Structural Evolution of a Large Explosive Caldera Volcano: Los Humeros México. PhD Thesis. University of Leicester, UK, pp. 485, 2011.

Wohletz, K., Civetta, L., and Orsi, G.: Thermal evolution of the Phlegraean magmatic system. J. Volcanol. Geoth. Res., 91, 381-414, 1999.

Wood, B. J.: The solubility of alumina in orthopyroxene coexisting with garnet. Contrib. Mineral. Petr., 46(1), 1-15, 1974.

Wotzlaw, J. R.-F., Bindeman, I. N., Watts, K. E., Schmitt, A. K., Caricchi, L. and Schaltegger, U.: Linking rapid magma reservoir assembly and eruption trigger mechanisms at evolved Yellowstone type supervolcanoes. Geology, 42, 807–810, 2014.

Wright, T. L., and Fiske, R. S.: Origin of the differentiated and hybrid lavas of Kilauea volcano, Hawaii. J. Petrol., 12, 1-65, 1971.

Yáñez, C., and García, S.: Exploración de la región geotérmica Los Humeros-Las Derrumbadas, Estados de Puebla y Veracruz, C.F.E. Mexico, Internal Report, 1-96, 1982.

Yang, H. J., Kinzler, R. J., and Grove, T. L.: Experiments and models of anhydrous, basaltic olivine-plagioclase-augite saturated melts from 0.001 to 10 kbar. Contrib. Mineral. Petr., 124, 1-18, 1996.

Yang, H. J., Frey, F. A., Clague, D. A., and Garcia, M. O.: Mineral chemistry of submarine lavas from Hilo Ridge, Hawaii: implications for magmatic processes within Hawaiian rift zones. Contrib. Mineral. Petr., 135, 355-372, 1999.

Zhang, J., Davidson, J. P., Humphreys, M. C. S., Macpherson, C. G., and Neill, I.: Magmatic enclaves and andesitic lavas from Mt. Lamington, Papua New Guinea: implications for recycling of earlier-fractionated minerals through magma recharge. J. Petrol., 56, 2223-2256, 2015.

Zheng, J., Mao, J., Chai, F., and Yang, F.: Petrogenesis of Permian A-type granitoids in the Cihai iron ore district, Eastern Tianshan, NW China: Constraints on the timing of iron mineralization and implications for a non-plume tectonic setting. Lithos, 260, 371-383, 2016.

Zhu, Y., and Ogasawara, Y.: Clinopyroxene phenocrysts (with green salite cores) in trachybasalts: implications for two magma chambers under the Kokchetav UHP massif, North Kazakhstan. J. Asian Earth Sci., 22, 517-527, 2004.

Solid Earth Discuss., https://doi.org/10.5194/se-2019-86
Manuscript under review for journal Solid Earth
Discussion started: 22 May 2019

1635 **SUPPLEMENTARY MATERIALS**

1636 *Supplementary Tables S1: Feldspar, EMPA complete dataset.*

1637 *Supplementary Table S2: Clinopyroxene, EMPA complete dataset.*

1638 *Supplementary Table S3: Olivine, EMPA complete dataset.*

1639 *Supplementary Table S4: Orthopyroxene, EMPA complete dataset.*

1640 *Supplementary Table S5: Opaque Minerals and Spinels, EMPA complete dataset.*

1641

Solid Earth Discuss., https://doi.org/10.5194/se-2019-86
Manuscript under review for journal Solid Earth
Discussion started: 22 May 2019

1642 **FIGURES**

1643 **Figure 1**

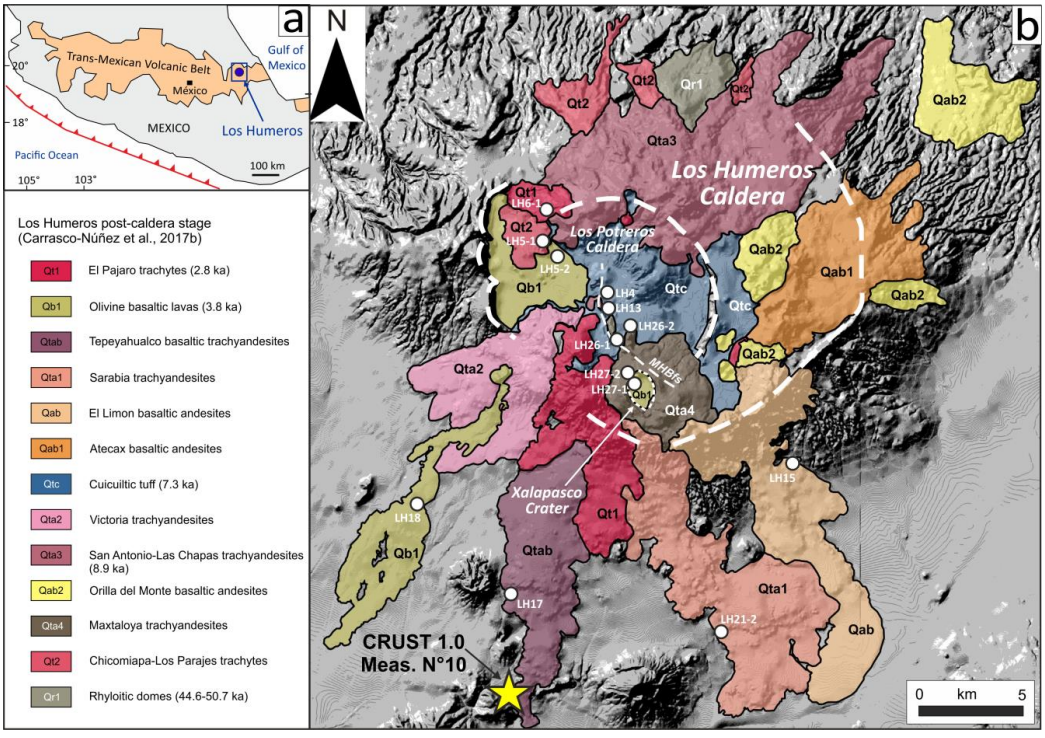

1644

1645 **Figure-1.** Geological Context. (a) The Los Humeros volcanic complex (LHVC, blue dot) with respect to the
1646 Trans-Mexican Volcanic Belt (TMVB). (b) Shaded relief image obtained from 15 m resolution digital
1647 elevation model (DEM) of the LHVC. Volcanic products of the Los Humeros post-caldera stage are redrawn
1648 from Carrasco-Núñez et al. (2017b). The map shows location (white dots) and volcanological significance of
1649 the samples used in this study. The yellow star indicates the locality of the measure N°10 of the Crust 1.0
1650 global model (Dziewonski and Anderson, 1981; Davies, 2013).

1651

1652

Solid Earth Discuss., https://doi.org/10.5194/se-2019-86
Manuscript under review for journal Solid Earth
Discussion started: 22 May 2019

1653 **Figure 2**

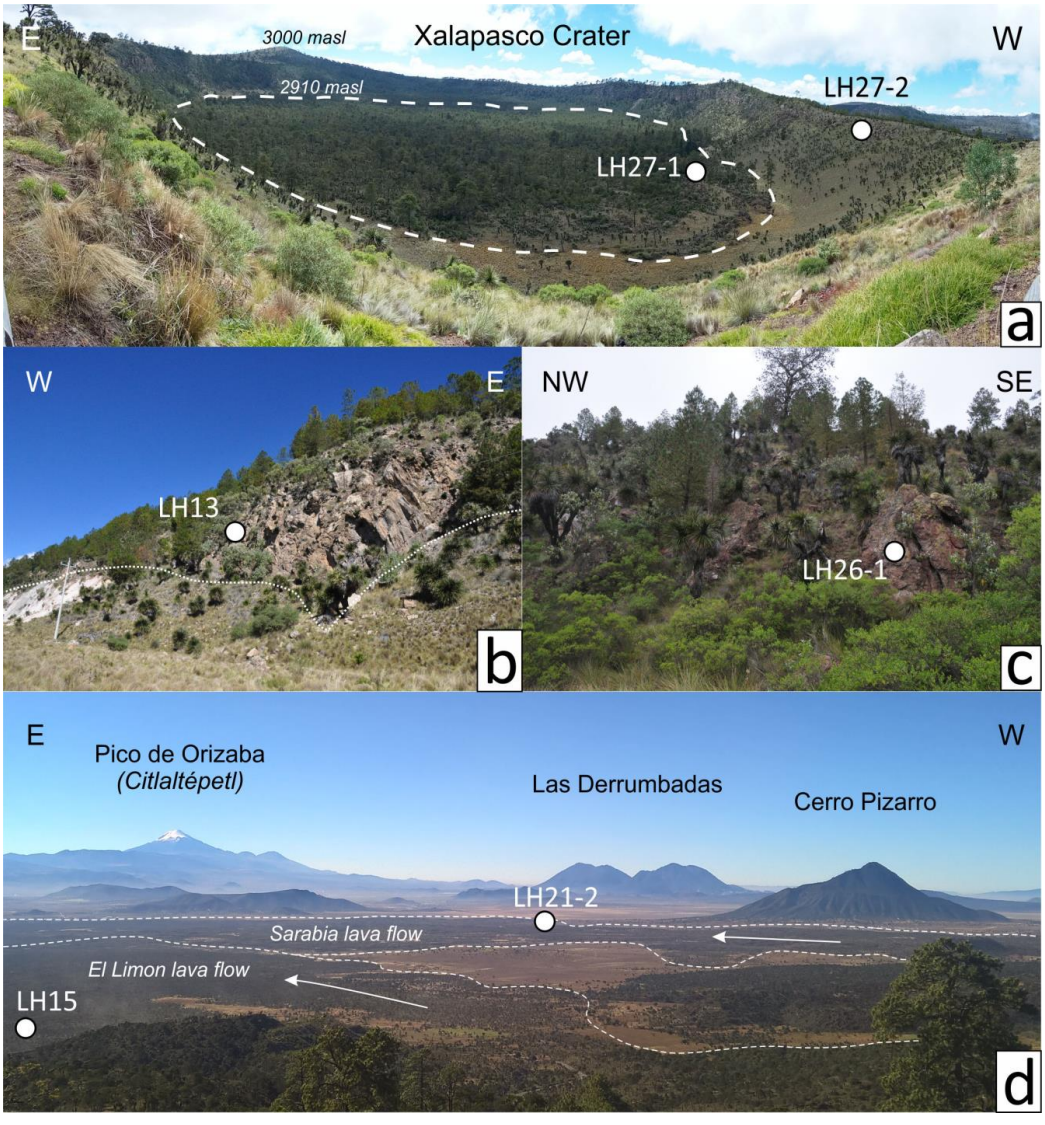

1654

1655 **Figure-2.** Field photographs of LHPCS volcanic products. (a) E-W panoramic view of Xalapasco crater; the
1656 white dashed line indicates the limit of Ol-basalts lavas filling the crater. (b) Trachyandesites lavas
1657 outcropping at Los Potreros, south to Los Humeros town. Joints are indicated with continue white lines. (c)
1658 Trachyandesites lava-dome outcropping inside Los Potreros caldera, north to Xalapasco crater. (d) E-W
1659 panoramic view from the Los Humeros caldera rim. With dashed lines are indicated the two major
1660 trachyandesitic lava flows of "El Limón" and "Sarabia". Pico de Orizaba, Las Derrumbadas and Cerro Pizarro
1661 volcanoes are also indicated. White dots indicate sampling localities.

1662

1663

Solid Earth Discuss., https://doi.org/10.5194/se-2019-86
Manuscript under review for journal Solid Earth
Discussion started: 22 May 2019

1664 **Figure 3**

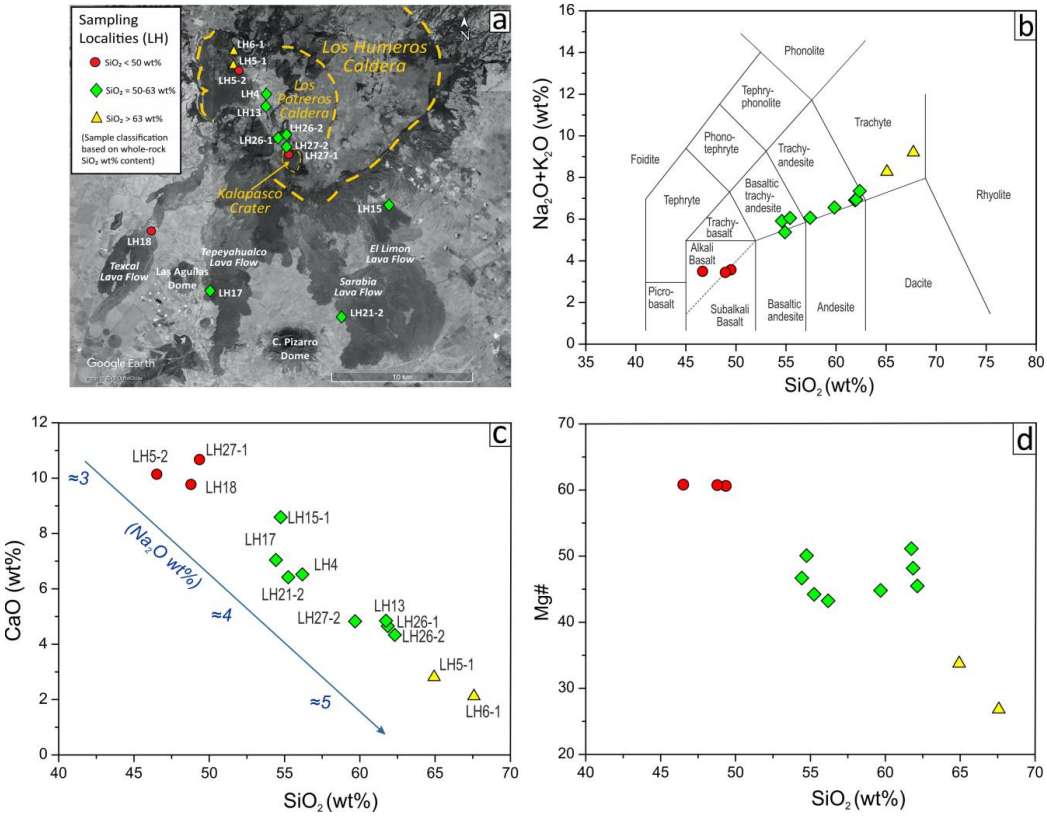

1665

1666 **Figure-3.** (a) Satellite image of the LHVC (Image Landsat from Google Earth Pro, 2018 Digital Globe;
1667 courtesy of Google) with localization of samples selected for this study. (b) Total alkali versus silica (TAS)
1668 diagram (Le Maitre et al., 2002). (c-d) Major elements selected Harker diagrams for LHPCS studied lavas.

1669

1670

Solid Earth Discuss., https://doi.org/10.5194/se-2019-86
Manuscript under review for journal Solid Earth
Discussion started: 22 May 2019

1671 **Figure 4**

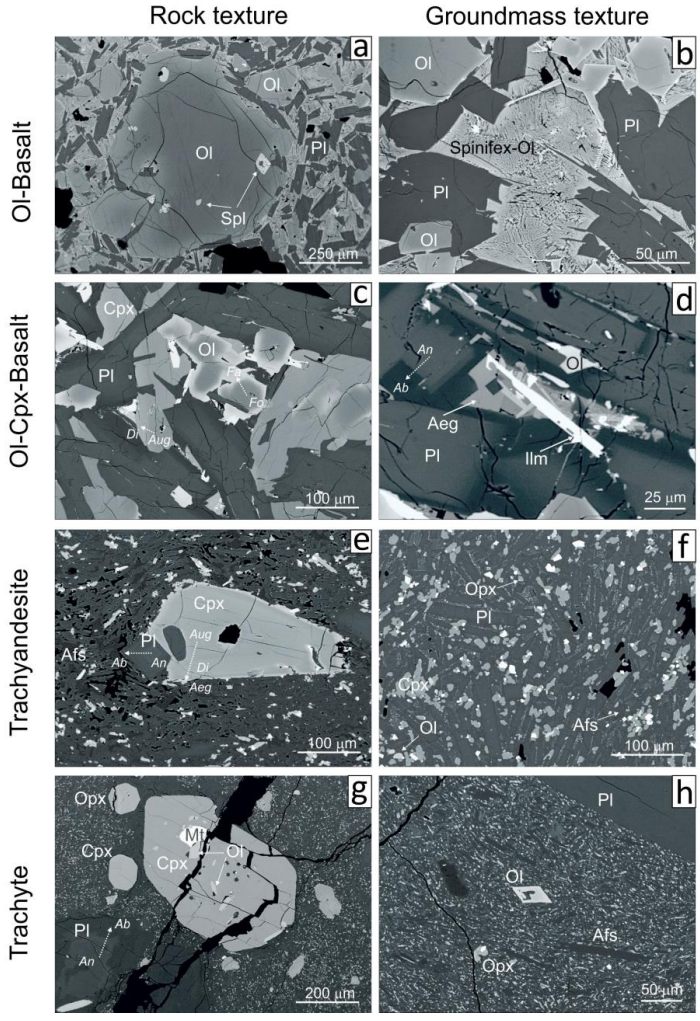

1672

1673 **Figure-4.** Microtextures and fabrics of the LHPCS lavas. (a) Back-scattered electrons (BSE) image of the Ol-
1674 basalt fabric, dominated by euhedral unzoned Pl+Ol, with major olivine phenocryst characterized by Cr-Spl
1675 inclusions. (b) BSE image of Ol-basalt groundmass highlighting the spinifex to skeletal and dendritic
1676 crystallization of olivine. (c) BSE image of Cpx-bearing Ol-basalt. Normal zoning growth is observed for all
1677 the three main mineral phases (Pl+Ol+Cpx). (d) BSE image of Cpx-bearing Ol-basalt groundmass
1678 characterized by albitic plagioclase, aegirine-pyroxene, Fe-rich olivine and ilmenite. (e-f) BSE images of
1679 trachyandesites. It is possible to observe a microcrystalline groundmass where major phenocrysts of Cpx
1680 and Pl are dispersed. (g-h) BSE images of trachytes, characterized by a microcrystalline groundmass and
1681 Pl+Cpx+Opx phenocrysts. Major Cpx phenocrysts present inclusion of Ol+Mt.

1682

Solid Earth Discuss., https://doi.org/10.5194/se-2019-86
Manuscript under review for journal Solid Earth
Discussion started: 22 May 2019

1683 **Figure 5**

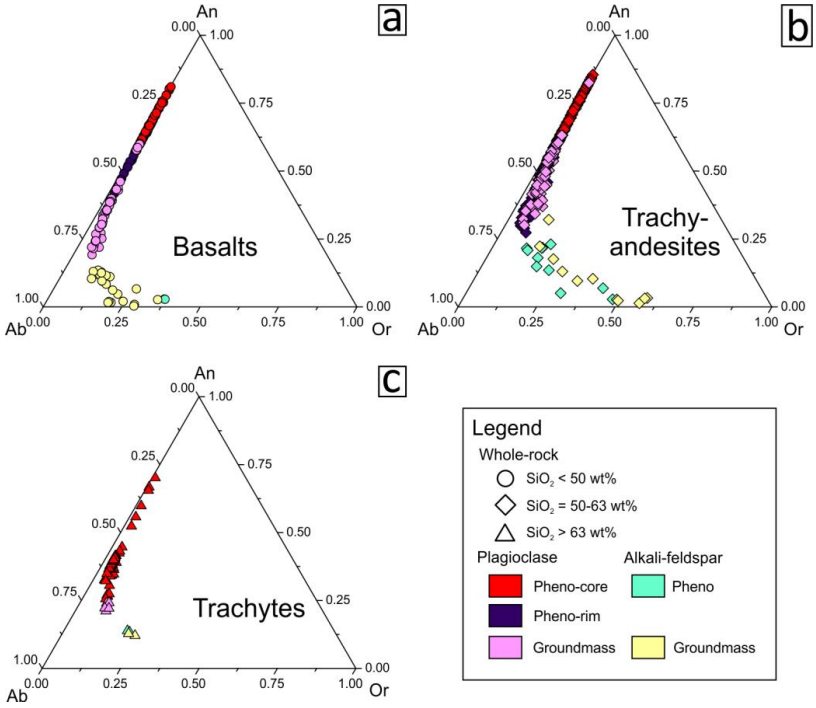

1684

1685 **Figure-5.** An-Ab-Or diagrams showing the composition of feldspar in (a) basalts (circles), (b) trachyandesites

1686 (diamonds) and (c) trachytes (triangles) of LHPCS lavas.

1687

Solid Earth Discuss., https://doi.org/10.5194/se-2019-86
Manuscript under review for journal Solid Earth
Discussion started: 22 May 2019

1688 **Figure 6**

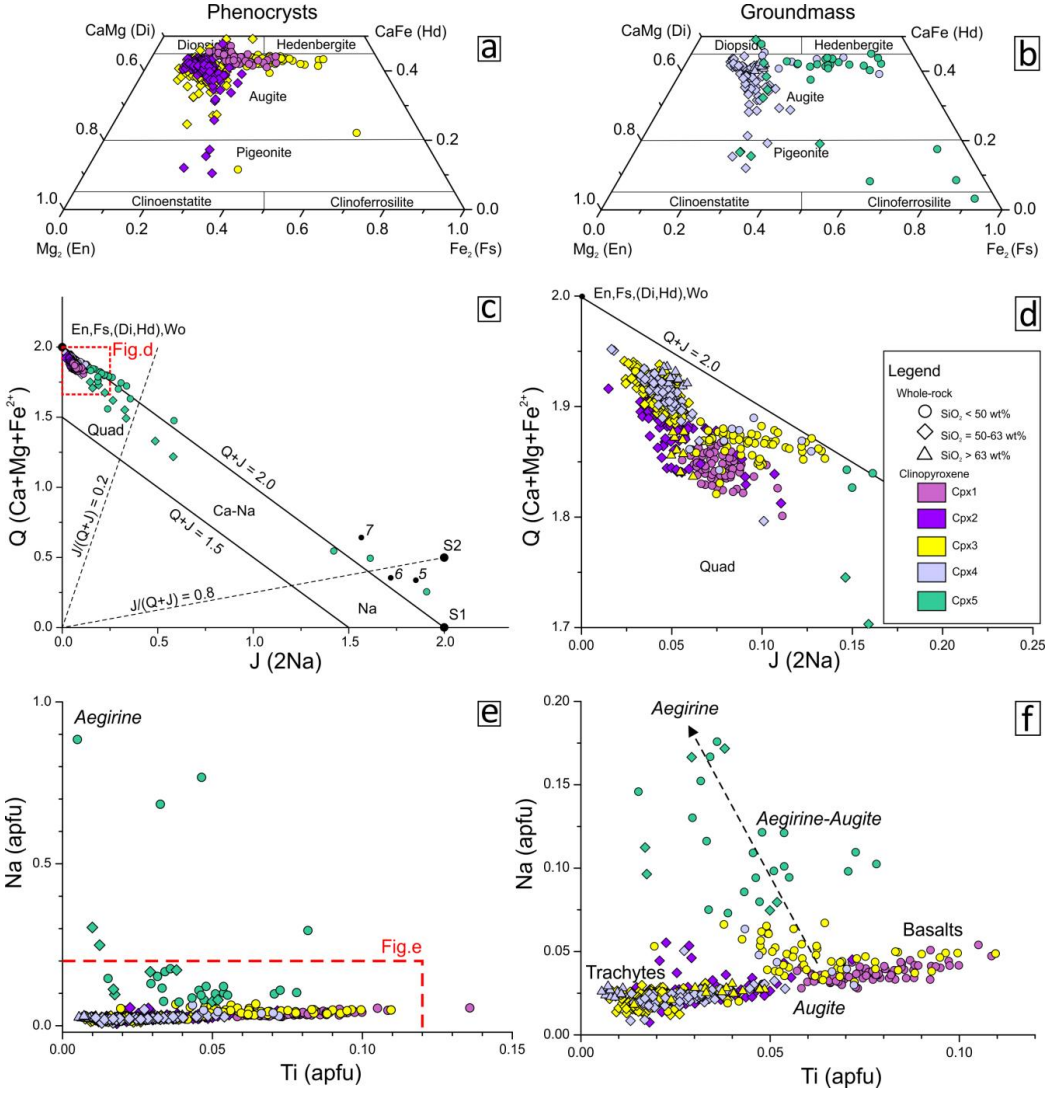

1689

1690 **Figure-6.** Di-Hd-En-Fs, Q-J and Ti vs. Na diagrams showing the composition of clinopyroxenes in LHPCS
1691 lavas. Basalt, trachyandesites and trachytes are indicated with circles, diamonds and trinagles, respectively.
1692 (a) Di-Hd-En-Fs diagram for clinopyroxene phenocrysts (Cpx1, Cpx2, Cpx3). (b) Di-Hd-En-Fs diagram for
1693 clinopyroxene microlites (Cpx4) and Na-clinopyroxenes (Cpx5). (c) Q-J diagram for pyroxenes with
1694 indication of end-members (Morimoto, 1989). (d) Enlargement of area indicated in (c). (e) Ti vs. Na diagram
1695 illustrating the compositional differences between clinopyroxenes. (f) Enlargement of area indicated in (e),
1696 showing the main Augite trend characterizing the evolution from basalts to trachytes and the divergent
1697 presence of Aegirine-Augite and Aegirine series.

1698

Solid Earth Discuss., https://doi.org/10.5194/se-2019-86
Manuscript under review for journal Solid Earth
Discussion started: 22 May 2019

1699 **Figure 7**

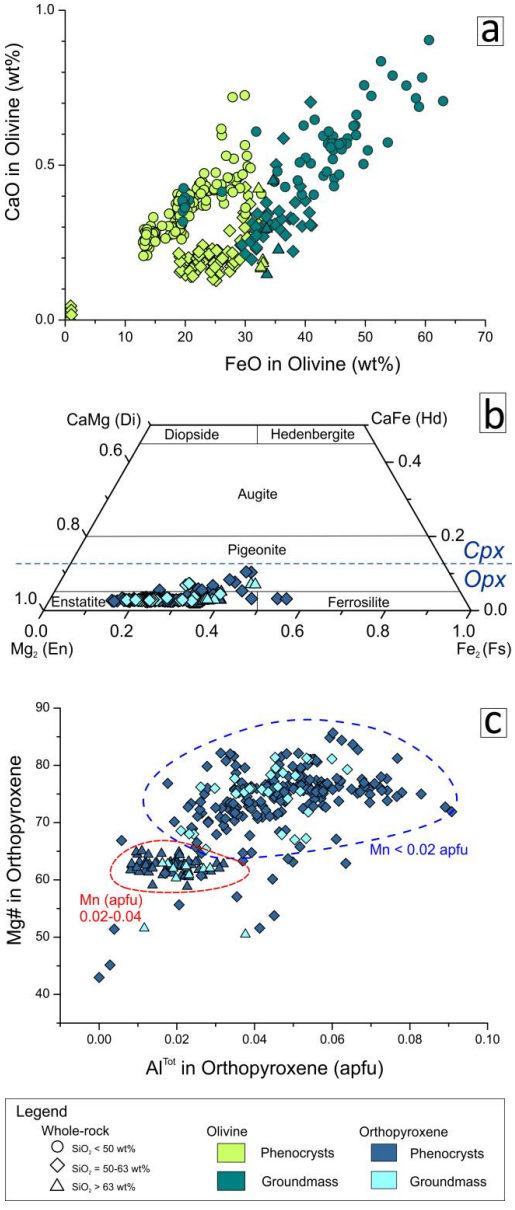

1700

1701 **Figure-7.** (a) CaO vs. FeO diagram showing the composition of olivine in LHPCS lavas. (b) Di-Hd-En-Fs
1702 diagram showing the orthopyroxene chemistry in LHPCS studied lavas. (c) Al vs Mg# diagram showing the
1703 main compositional differences between orthopyroxene populations from trachytes and trachyandesites.
1704 Mn (apfu) contents are also reported.

1705

1706

Solid Earth Discuss., https://doi.org/10.5194/se-2019-86
Manuscript under review for journal Solid Earth
Discussion started: 22 May 2019

1707 **Figure 8**

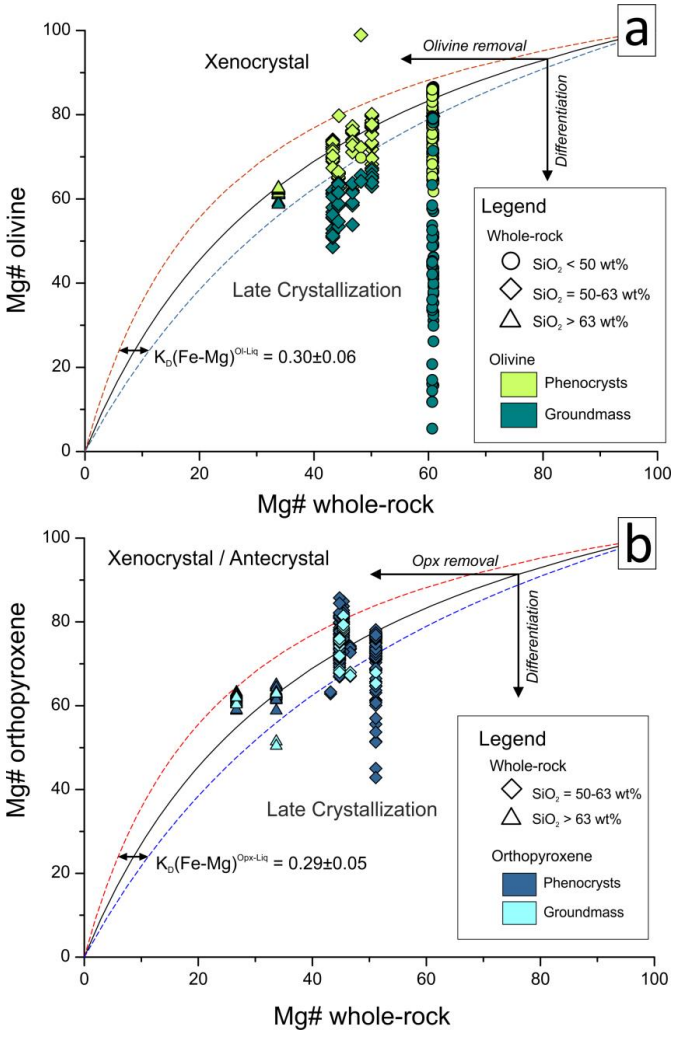

1708

1709 **Figure-8.** Rhodes diagrams showing the results of test of equilibrium liquid and olivine (a) and
1710 orthopyroxene (b). The partitioning of Fe-Mg between mineral and liquid (Fe-Mg exchange coefficient) or
1711 $K_D^{min\text{-}liq}$(Fe-Mg) is shown (black lines). The accepted range of equilibrium constant values for both figures (a)
1712 and (b) is indicated by dashed lines. $K_D^{min\text{-}liq}$(Fe-Mg) values are from Putirka (2008). Nominal melt
1713 compositions for clinopyroxene are selected from whole-rock. Vectors of olivine removal from melt and
1714 closed system differentiation are redrawn after Putirka (2008 and references therein). Fields of
1715 Xenocrystal/Antecrystals and Late Crystallization are also indicated. Symbols and colors refer to Fig. 7.
1716
1717

Solid Earth Discuss., https://doi.org/10.5194/se-2019-86
Manuscript under review for journal Solid Earth
Discussion started: 22 May 2019

1718 **Figure 9**

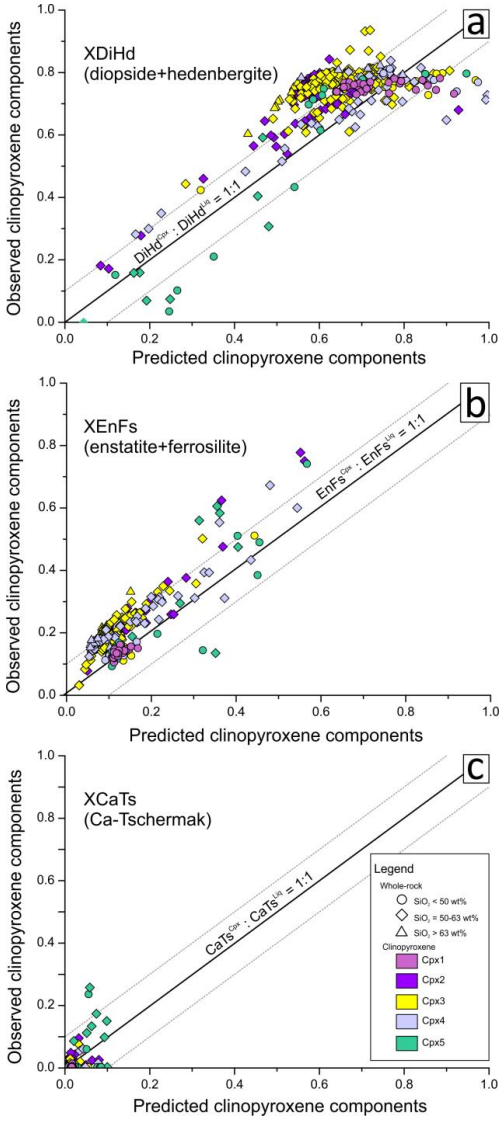

1719

1720

1721 **Figures-9.** Clinopyroxene-melt equilibrium tests: (a) DiHd: diopside-hedenbergite, (b) EnFs: enstatite-
1722 ferrosilite, and (c) CaTs: Ca-Tschermak components. Equilibrium associated with observed components in
1723 pyroxenes are paired with predicted components in respective hosting-melts. The accepted range of
1724 equilibrium is indicated in each figure by dashed lines. Nominal melt compositions for clinopyroxene are
1725 selected from whole-rock. Symbols and colors refer to Fig. 6.

1726

1727

Solid Earth Discuss., https://doi.org/10.5194/se-2019-86
Manuscript under review for journal Solid Earth
Discussion started: 22 May 2019

1728 **Figure 10**

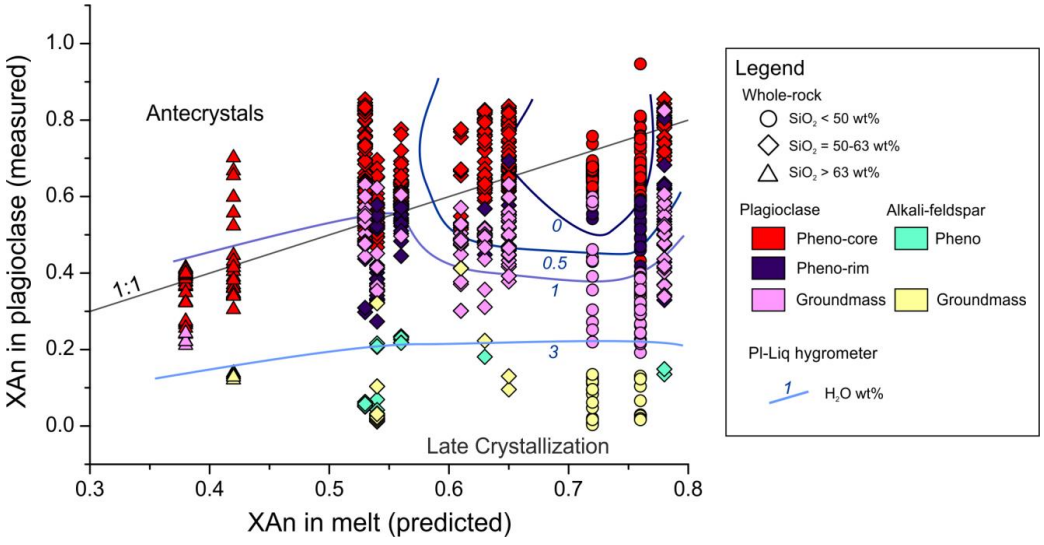

1729

1730

1731 **Figure-10.** Plagioclase-melt equilibrium test. Equilibrium associated with anorthite (XAn) component in
1732 plagioclase are paired with predicted anorthite in melt. Nominal melt compositions for clinopyroxene are
1733 selected from whole-rock. Calculated water concentrations using plagioclase-melt hygromether (Putirka,
1734 2008) are reported in diagrams with isolines (graded blue lines). Symbols and colors refer to Fig. 5.

1735

1736

1737

1738

Solid Earth Discuss., https://doi.org/10.5194/se-2019-86
Manuscript under review for journal Solid Earth
Discussion started: 22 May 2019

1739 **Figure 11**

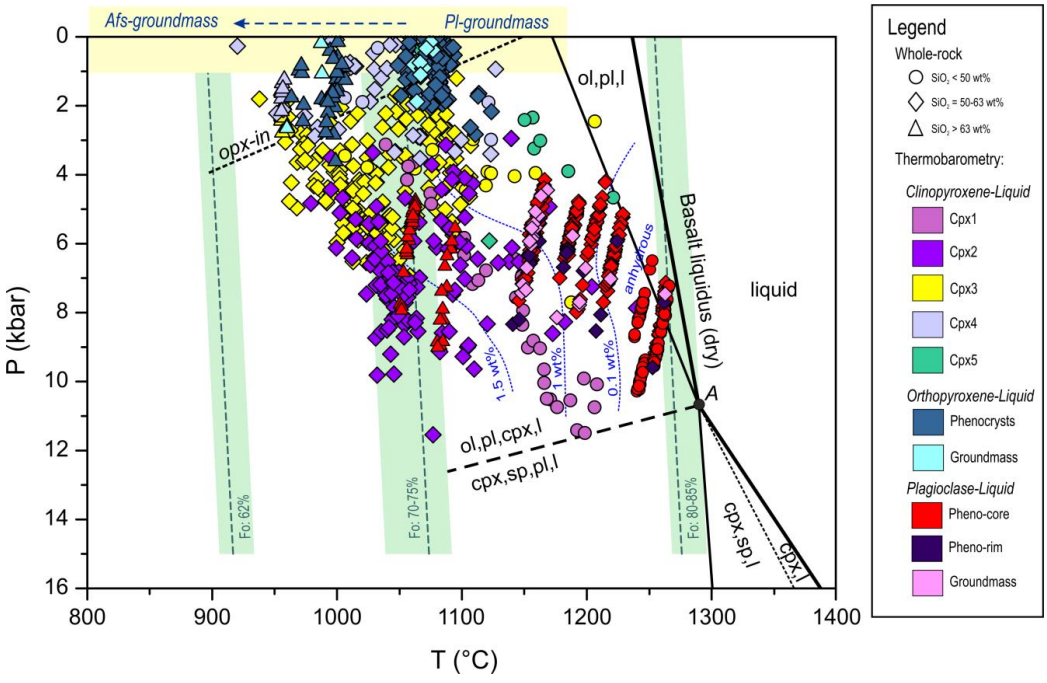

1740
1741

1742 **Figure-11.** A summary of the results obtained from thermobarometry models applied to Los Humeros post-
1743 caldera stage lavas. Symbols refer to whole-rock chemistry compositions, whereas colors of different
1744 phases refer to mineral chemistry diagrams. Green-shaded field shows the results of olivine-liquid
1745 thermometry. Blue dashed isolines represent the results of plagioclase-melt hygrometer. Yellow-shaded
1746 field indicates pressure-temperature domain of crystallization of feldspars in groundmass. Basalt liquidus
1747 curve, ol+cpx+ol+sp+l stability fields and point "A" (basalt liquidus in equilibrium with mantle peridotite
1748 mineral assemblage of ol+cpx) are redrawn after Grove (2000). Opx-in stability curve is redrawn after
1749 Wallace and Anderson (2000).
1750
1751
1752
1753

Solid Earth Discuss., https://doi.org/10.5194/se-2019-86
Manuscript under review for journal Solid Earth
Discussion started: 22 May 2019

1754 **Figure 12**

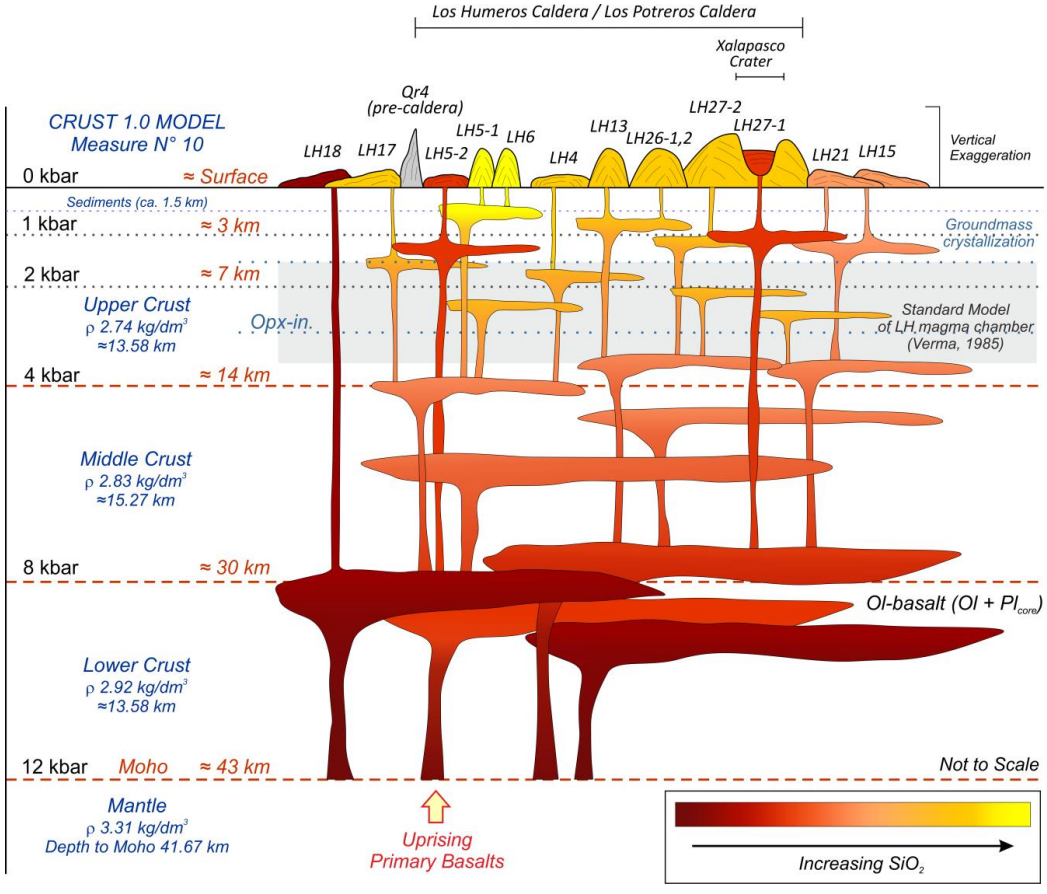

1755
1756

1757 **Figure-12.** Schematic representation (not to scale) of the magmatic plumbing system feeding LHPCS
1758 activity, beneath Los Humeros caldera as derived by pressure-temperature estimates obtained from
1759 mineral-liquid thermobarometry models. The conceptual model is integrated with the crustal structure of
1760 the study area as derived by the Measure N°10 of the Crust 1.0 global Model (Davies, 2013). Grey shaded
1761 field indicates the depth and thickness of the existing conceptual model of a single, huge classical magma
1762 chamber proposed by Verma (1985a, 1985b).
1763
1764

Solid Earth Discuss., https://doi.org/10.5194/se-2019-86
Manuscript under review for journal Solid Earth
Discussion started: 22 May 2019

1765 **Table 1**

Table 1 - Major element bulk-rock compositions of LHPCS studied lava samples.

Rock type	Alkali-Basalts			Trachyandesites								Trachytes	
Sample	LH5-2	LH18	LH27-1	LH17	LH15-1	LH21-2	LH4	LH27-2	LH13	LH26-1	LH26-2	LH5-1	LH6-1
SiO_2, wt%	46.51	48.78	49.35	54.43	54.74	55.24	56.18	59.69	61.74	61.85	62.14	64.93	67.58
TiO_2	1.471	1.490	1.372	1.394	1.075	1.561	1.375	1.016	0.882	0.889	0.933	0.738	0.605
Al_2O_3	16.23	16.17	17.11	16.33	20.68	15.99	16.57	17.39	15.68	15.70	16.82	15.47	15.83
$Fe_2O_3^{tot}$	10.78	10.62	10.26	8.08	6.49	8.62	7.88	5.76	5.15	5.22	5.32	4.58	3.73
MnO	0.161	0.160	0.155	0.123	0.092	0.133	0.114	0.087	0.085	0.085	0.095	0.077	0.074
MgO	8.44	8.29	7.97	3.57	3.28	3.45	2.90	2.36	2.72	2.45	2.24	1.18	0.69
CaO	10.14	9.77	10.67	7.04	8.59	6.42	6.52	4.83	4.85	4.66	4.52	2.81	2.12
Na_2O	3.11	2.98	3.21	4.10	3.68	4.14	3.96	4.31	4.19	4.31	4.30	4.79	5.26
K_2O	0.33	0.41	0.30	1.76	1.64	1.86	1.99	2.20	2.67	2.58	2.76	3.44	3.89
P_2O_5	0.19	0.21	0.17	0.32	0.26	0.34	0.34	0.27	0.25	0.23	0.22	0.18	0.13
LOI	1.90	0.81	-0.35	0.90	0.49	0.52	1.19	1.55	0.50	0.93	0.70	0.73	0.31
Total (wt%)	99.27	99.68	100.20	98.05	101.01	98.29	99.02	99.47	98.72	98.91	100.10	98.92	100.20
Mg#	61	61	61	47	50	44	43	45	51	48	45	34	27

Note: LOI - loss on ignition; Mg# - molar [$Mg^*100/(Mg + Fe^{tot})$].

1766

1767